Statistical Analysis. Values are expressed as the mean ± SE. An unpaired *t* test (for two groups) or ANOVA with the Bonferroni correction (for more than three groups) was used to evaluate the differences of the averages, unless otherwise noted.

1. Alvarez-Buylla, A. & Lim, D. A. (2004) *Neuron* **41**, 683–686.
2. Okano, H. (2002) *J. Neurosci. Res.* **69**, 698–707.
3. Lie, D. C., Song, H., Colamarino, S. A., Ming, G. L. & Gage, F. H. (2004) *Annu. Rev. Pharmacol. Toxicol.* **44**, 399–421.
4. Lois, C. & Alvarez-Buylla, A. (1993) *Proc. Natl. Acad. Sci. USA* **90**, 2074–2077.
5. Levison, S. W. & Goldman, J. E. (1993) *Neuron* **10**, 201–212.
6. Luskin, M. B. (1993) *Neuron* **11**, 173–189.
7. Altman, J. & Das, G. D. (1965) *J. Comp. Neurol.* **124**, 319–335.
8. Bayer, S. A., Yackel, J. W. & Puri, P. S. (1982) *Science* **216**, 890–892.
9. Eriksson, P. S., Perfilieva, E., Bjork-Eriksson, T., Alborn, A. M., Nordborg, C., Peterson, D. A. & Gage, F. H. (1998) *Nat. Med.* **4**, 1313–1317.
10. van Praag, H., Schinder, A. F., Christie, B. R., Toni, N., Palmer, T. D. & Gage, F. H. (2002) *Nature* **415**, 1030–1034.
11. Carleton, A., Petreanu, L. T., Lansford, R., Alvarez-Buylla, A. & Lledo, P. M. (2003) *Nat. Neurosci.* **6**, 507–518.
12. Gheusi, G., Cremer, H., McLean, H., Chazal, G., Vincent, J. D. & Lledo, P. M. (2000) *Proc. Natl. Acad. Sci. USA* **97**, 1823–1828.
13. Nakatomi, H., Kuriu, T., Okabe, S., Yamamoto, S., Hatano, O., Kawahara, N., Tamura, A., Kirino, T. & Nakafuku, M. (2002) *Cell* **110**, 429–441.
14. Reya, T., Morrison, S. J., Clarke, M. F. & Weissman, I. L. (2001) *Nature* **414**, 105–111.
15. Takakura, N., Kodama, H. & Nishikawa, S. (1996) *J. Exp. Med.* **184**, 2301–2309.
16. Ueno, H., Sakita-Ishikawa, M., Morikawa, Y., Nakano, T., Kitamura, T. & Saito, M. (2003) *Nat. Immunol.* **4**, 457–463.
17. Reynolds, B. A. & Weiss, S. (1992) *Science* **255**, 1707–1710.
18. Fung, E. T., Thulasiraman, V., Weinberger, S. R. & Dalmasso, E. A. (2001) *Curr. Opin. Biotechnol.* **12**, 65–69.
19. Teichberg, V. I., Silman, I., Beitsch, D. D. & Resheff, G. (1975) *Proc. Natl. Acad. Sci. USA* **72**, 1383–1387.
20. Barondes, S. H., Castronovo, V., Cooper, D. N., Cummings, R. D., Drickamer, K., Feizi, T., Gitt, M. A., Hirabayashi, J., Hughes, C., Kasai, K., *et al.* (1994) *Cell* **76**, 597–598.
21. Perillo, N. L., Marcus, M. E. & Baum, L. G. (1998) *J. Mol. Med.* **76**, 402–412.
22. Leffler, H. (2001) *Results Probl. Cell Differ.* **33**, 57–83.
23. Capela, A. & Temple, S. (2002) *Neuron* **35**, 865–875.
24. Mercier, F., Kitasako, J. T. & Hatton, G. I. (2002) *J. Comp. Neurol.* **451**, 170–188.
25. Yanagisawa, M., Liour, S. S. & Yu, R. K. (2004) *J. Neurochem.* **91**, 804–812.
26. Pipia, G. G. & Long, M. W. (1997) *Nat. Biotechnol.* **15**, 1007–1011.
27. Vas, V., Fajka-Boja, R., Ion, G., Dudics, V., Monostori, E. & Uher, F. (2005) *Stem Cells* **23**, 279–287.
28. Tropepe, V., Sibilia, M., Ciruna, B. G., Rossant, J., Wagner, E. F. & van der Kooy, D. (1999) *Dev. Biol.* **208**, 166–188.
29. Horie, H., Inagaki, Y., Sohma, Y., Nozawa, R., Okawa, K., Hasegawa, M., Muramatsu, N., Kawano, H., Horie, M., Koyama, H., *et al.* (1999) *J. Neurosci.* **19**, 9964–9974.
30. Poirier, F. & Robertson, E. J. (1993) *Development (Cambridge, U.K.)* **119**, 1229–1236.
31. Joubert, R., Kuchler, S., Zanetta, J. P., Bladier, D., Avellana-Adalid, V., Caron, M., Doinel, C. & Vincendon, G. (1989) *Dev. Neurosci.* **11**, 397–413.
32. Brown, D. C. & Gatter, K. C. (1990) *Histopathology* **17**, 489–503.
33. Seri, B., Garcia-Verdugo, J. M., McEwen, B. S. & Alvarez-Buylla, A. (2001) *J. Neurosci.* **21**, 7153–7160.
34. Doetsch, F., Caille, I., Lim, D. A., Garcia-Verdugo, J. M. & Alvarez-Buylla, A. (1999) *Cell* **97**, 703–716.
35. Parras, C. M., Galli, R., Britz, O., Soares, S., Galichet, C., Battiste, J., Johnson, J. E., Nakafuku, M., Vescovi, A. & Guillemot, F. (2004) *Embo. J.* **23**, 4495–4505.
36. Doetsch, F., Petreanu, L., Caille, I., Garcia-Verdugo, J. M. & Alvarez-Buylla, A. (2002) *Neuron* **36**, 1021–1034.
37. Morshead, C. M., Reynolds, B. A., Craig, C. G., McBurney, M. W., Staines, W. A., Morassutti, D., Weiss, S. & van der Kooy, D. (1994) *Neuron* **13**, 1071–1082.
38. Whitney, P. L., Powell, J. T. & Sanford, G. L. (1986) *Biochem. J.* **238**, 683–689.
39. Inagaki, Y., Sohma, Y., Horie, H., Nozawa, R. & Kadoya, T. (2000) *Eur. J. Biochem.* **267**, 2955–2964.
40. Yu, C. C. & Filipe, M. I. (1993) *Histochem. J.* **25**, 843–853.
41. Shi, Y., Chichung Lie, D., Taupin, P., Nakashima, K., Ray, J., Yu, R. T., Gage, F. H. & Evans, R. M. (2004) *Nature* **427**, 78–83.
42. Tramontin, A. D., Garcia-Verdugo, J. M., Lim, D. A. & Alvarez-Buylla, A. (2003) *Cereb. Cortex* **13**, 580–587.
43. Alvarez-Buylla, A., Garcia-Verdugo, J. M. & Tramontin, A. D. (2001) *Nat. Rev. Neurosci.* **2**, 287–293.
44. Poirier, F., Timmons, P. M., Chan, C. T., Guenet, J. L. & Rigby, P. W. (1992) *Development (Cambridge, U.K.)* **115**, 143–155.
45. Colnot, C., Fowlis, D., Ripoche, M. A., Bouchaert, I. & Poirier, F. (1998) *Dev. Dyn.* **211**, 306–313.
46. Puche, A. C., Poirier, F., Hair, M., Bartlett, P. F. & Key, B. (1996) *Dev. Biol.* **179**, 274–287.
47. Schofield, R. (1978) *Blood Cells* **4**, 7–25.
48. Spradling, A., Drummond-Barbosa, D. & Kai, T. (2001) *Nature* **414**, 98–104.
49. Campos, L. S., Leone, D. P., Relvas, J. B., Brakebusch, C., Fassler, R., Suter, U. & Ffrench-Constant, C. (2004) *Development (Cambridge, U.K.)* **131**, 3433–3444.
50. Emsley, J. G. & Hagg, T. (2003) *Exp. Neurol.* **183**, 273–285.
51. Liu, F. T. & Rabinovich, G. A. (2005) *Nat. Rev. Cancer* **5**, 29–41.
52. Wells, V. & Mallucci, L. (1991) *Cell* **64**, 91–97.
53. Shimazaki, T., Shingo, T. & Weiss, S. (2001) *J. Neurosci.* **21**, 7642–7653.
54. Shingo, T., Gregg, C., Enwere, E., Fujikawa, H., Hassam, R., Geary, C., Cross, J. C. & Weiss, S. (2003) *Science* **299**, 117–120.

NEUROSCIENCE

nature
medicine

Conditional ablation of Stat3 or Socs3 discloses a dual role for reactive astrocytes after spinal cord injury

Seiji Okada[1-3], Masaya Nakamura[4], Hiroyuki Katoh[4], Tamaki Miyao[1], Takuya Shimazaki[1], Ken Ishii[4], Junichi Yamane[1,4], Akihiko Yoshimura[5], Yukihide Iwamoto[2], Yoshiaki Toyama[4] & Hideyuki Okano[1,3]

In the injured central nervous system (CNS), reactive astrocytes form a glial scar and are considered to be detrimental for axonal regeneration, but their function remains elusive. Here we show that reactive astrocytes have a crucial role in wound healing and functional recovery by using mice with a selective deletion of the protein signal transducer and activator of transcription 3 (Stat3) or the protein suppressor of cytokine signaling 3 (Socs3) under the control of the Nes promoter-enhancer (Nes-Stat3−/−, Nes-Socs3−/−). Reactive astrocytes in Nes-Stat3−/− mice showed limited migration and resulted in markedly widespread infiltration of inflammatory cells, neural disruption and demyelination with severe motor deficits after contusive spinal cord injury (SCI). On the contrary, we observed rapid migration of reactive astrocytes to seclude inflammatory cells, enhanced contraction of lesion area and notable improvement in functional recovery in Nes-Socs3−/− mice. These results suggest that Stat3 is a key regulator of reactive astrocytes in the healing process after SCI, providing a potential target for intervention in the treatment of CNS injury.

Because the regenerative capability of the mammalian CNS is poor, limited functional recovery occurs during the chronic phase of SCI. At the subacute phase of SCI, however, gradual functional recovery is observed to some extent in both rodents and humans (except in cases of complete paralysis). The mechanism behind this functional recovery remains unclear. Here, we investigated this issue by focusing on the action of reactive astrocytes in a mouse model of SCI.

To interpret the process of paralysis improvement in the subacute phase, we examined serial histological sections of contused spinal cords and followed motor function for 6 weeks after injury in wild-type mice and found that the area of neural cell loss gradually enlarged in a rostral-caudal direction within a few days after SCI (acute phase) and a portion of Hu-expressing neurons were positive for cleaved caspase-3, indicating that the secondary injury process lasted for several days in this model (Supplementary Fig. 1 online) during which we observed limited functional recovery (Fig. 1a). Astrocytes surrounding the

lesion underwent a typical change of hypertrophy, process extension and increased expression of intermediate filaments such as GFAP and Nestin by 7 d after SCI (Fig. 1b), characteristic of 'reactive astrocytes.' Notably, these astrocytes eventually migrated centripetally to the lesion epicenter and gradually compacted the CD11b+ inflammatory cells, contracting the lesion area up until 14 d after SCI (subacute phase; Fig. 1c,d). During this process, we observed repair of injured tissue and gradual functional improvement, and reactive astrocytes formed a physical barrier against inflammatory cells, commonly referred to as glial scar. After the migration of reactive astrocytes and completion of glial scar (reactive gliosis), functional improvement reached a plateau around 2 weeks after injury (Fig. 1a,c). Although the glial scar has a crucial part in the lack of axonal regeneration in the chronic phase of SCI[1], our data strongly suggest that the emergence and migration of reactive astrocytes have a prominent role in the repair of injured tissue and the restoration of motor function in the subacute phase (before completion of the glial scar).

To confirm that the compaction of the lesion results from migration and not from proliferation of reactive astrocytes, we labeled proliferating cells with bromodeoxyuridine (BrdU). Analysis of mice that received a single injection of BrdU at 7 d after SCI showed that the population of BrdU+ cells was composed of reactive astrocytes and inflammatory cells, which were gradually compacted to the lesion center as time progressed (Fig. 1e and Supplementary Fig. 2 online). Analysis of mice that received daily injections of BrdU showed limited astrocyte proliferation after 7 d postinjury, suggesting that the development of reactive gliosis is mainly brought about by cellular hypertrophy and upregulation of GFAP of the astrocytes surrounding the lesion (Fig. 1f,g).

To address the regulatory mechanisms behind the reactive response of astrocytes, we investigated the role of Stat3 signaling (Figs. 2 and 3). Stat3 is a principal mediator in a variety of biological processes[2-4] including cancer progression, wound healing and the movement of various types of cells. In addition, Stat3 mediates certain aspects of astrogliosis downstream of the action of cytokines such as interleukin (IL)-6, leukemia inhibitory factor (LIF) and ciliary neurotrophic factor (CNTF) after CNS injury[5-8].
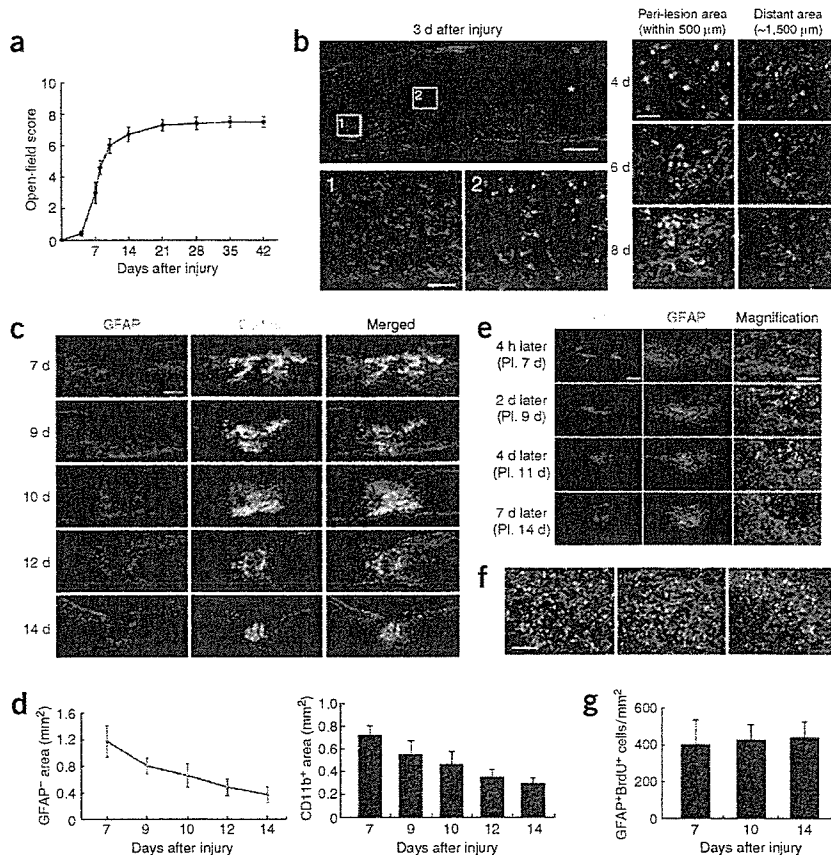
Figure 1 Migration of reactive astrocytes and compaction of inflammatory cells in wild-type mice. (a) Time course of lower limb functional recovery after SCI ($n = 10$). There was gradual recovery in the subacute phase. Data are mean ± s.e.m. (b) Phosphorylated Stat3 (green) and morphological changes were observed in GFAP$^+$ astrocytes (red) close to the lesion (boxed area 2) but not in distant areas (boxed area 1) at 3, 4, 6 and 8 d after SCI. Scale bar, 500 μm (upper left panel), 100 μm (lower left panel) and 50 μm (right panels). Asterisk indicates the lesion epicenter. (c) Time course of GFAP$^+$ reactive astrocytes and CD11b$^+$ cells. Reactive astrocytes gradually confine the area of inflammatory cell infiltration. Scale bar, 500 μm. (d) Quantitative analysis of GFAP$^-$ area (surrounded by reactive astrocytes) and CD11b$^+$ area ($n = 3$ per each time point). Data are mean ± s.d. (e) BrdU-labeled cells migrated toward the lesion epicenter. Mice were injected with BrdU (100 μg/g body weight) at 7 d after injury and killed 4 h, 2 d, 4 d, 7 d later. Scale bar, 500 μm and 100 μm. (f) The proliferating reactive astrocytes were labeled by daily injection of BrdU from the day of injury till killing at 7 (left), 10 (middle) and 14 d (right) after injury. GFAP, red; BrdU, green. Scale bar, 100 μm. (g) There were no differences in the number of GFAP$^+$BrdU$^+$ cells from 7 to 14 d after injury ($n = 3$ per group). Data are mean ± s.d.

In the injured spinal cord, phosphorylated Stat3 prominently increased at 12 h after injury, which remained detectable for 2 weeks (Fig. 3a). We observed phosphorylation and nuclear translocation of Stat3 mainly in reactive astrocytes surrounding the lesion, but not in distant areas for several days after injury (Fig. 1b and Supplementary Fig. 1). To elucidate the role of Stat3 in reactive astrocytes, we selectively disrupted the Stat3 gene under the control of Nes gene promoter and second intronic enhancer, which are activated in reactive astrocytes after SCI[9,10]. We created conditional knockout mice (Nes-Stat3$^{-/-}$) by crossing Stat3^{loxP} mice[11] with Nes-Cre transgenic mice[12], as embryonic lethality ensues in Stat3-null mice. Nes-Stat3$^{-/-}$ mice showed no apparent abnormalities in motor function and development, although they showed signs of hyperphagia and leptin resistance[13]. To identify the cells that underwent Cre-mediated recombination, we crossed another transgenic line[14] carrying a reporter gene construct, CAG promoter-loxP-CAT-loxP-EGFP (CAG-CAT$^{loxP/loxP}$-EGFP), which directs the expression of EGFP upon Cre-mediated recombination. After SCI, we observed high Cre-mediated expression of EGFP from reactive astrocytes surrounding the lesion, but not from neurons or oligodendrocytes (Supplementary Figs. 3 and 4 online), indicating recombination only in reactive astrocytes in both littermates and Nes-Stat3$^{-/-}$ mice.

At 2 weeks after injury, Nes-Stat3$^{-/-}$ mice showed markedly widespread infiltration of CD11b$^+$ inflammatory cells and demyelination compared to wild-type littermates (Fig. 2a). Notably, although the development of glial scar was observed around the injury site several days after injury in Nes-Stat3$^{-/-}$ mice (Fig. 2a,b and Supplementary Fig. 3), the configuration of these cells remained relatively unchanged for the following 6 weeks owing to their limited migration, resulting in

widespread demyelination and severe motor deficits (Fig. 2). Quantifications of GFAP$^-$ area and CD11b$^+$ area in wild-type littermates and Nes-Stat3$^{-/-}$ mice were comparable at 7 d after injury, implying a similar degree of astrocyte loss owing to secondary injury, but marked differences developed during the following 7 d, suggesting that Stat3 has a large impact on the migration of astrocytes rather than their survival after SCI (Fig. 2c). The progressive compaction of GFAP$^+$EGFP$^+$ cells toward the lesion center observed in wild-type littermates did not occur in Nes-Stat3$^{-/-}$ mice, providing further evidence of Stat3-dependent migration of reactive astrocytes (Fig. 2d). Confocal imaging confirmed the emergence of reactive astrocytes without phosphorylated Stat3 in Nes-Stat3$^{-/-}$ mice (Fig. 2e), indicating that the Stat3 activation is not necessarily indispensable for the appearance of reactive astrocytes or for the upregulation of Gfap and Nes. These data suggest that Stat3 is a key molecule for the migratory function of reactive astrocytes, which may be deeply involved in tissue repair and functional recovery after SCI (Fig. 2).

To further investigate the relationship between Stat3 signaling and function of reactive astrocytes, we analyzed SCI in Nes-Socs3$^{-/-}$ mice[15]. Socs3 is the negative feedback molecule of Stat3 and the 'bipolar' relationship between Stat3 and Socs3 has been noted in several selective deletion experiments[13,15,16]. In the injured spinal cord of Nes-Socs3$^{-/-}$ mice, phosphorylation of Stat3 was significantly greater and prolonged compared to that in wild-type mice, and immunohistochemistry confirmed greater expression of phosphorylated Stat3 in reactive astrocytes (Fig. 3a–c). Notably, the rapid development of reactive gliosis that compacted inflammatory cells in the injured spinal cord of Nes-Socs3$^{-/-}$ mice was observed as early as 7 d after injury (Fig. 3d,e). GFAP$^-$ area and CD11b$^+$ area were significantly reduced in Nes-Socs3$^{-/-}$ mice at 7 d after injury, during which Nes-Socs3$^{-/-}$ mice showed marked improvement of motor function compared to littermates (Fig. 3f,g). The differences in the area between wild-type

Figure 2 Compaction of inflammatory cells by reactive astrocytes and functional recovery were limited in *Nes-Stat3⁻/⁻* mice after SCI. (a) At 2 weeks after SCI, the infiltration of CD11b⁺ cells, GFAP⁻ area and demyelination were greater in *Nes-Stat3⁻/⁻* mice compared to wild-type (WT) littermates. Scale bars, 500 µm (upper left panel) and 300 µm (lower left panel). (b) The areas negative for Hu and GFAP were large in *Nes-Stat3⁻/⁻* mice even at 6 weeks after injury. Scale bar, 500 µm. (c) Comparison of GFAP⁻ area, CD11b⁺ area and LFB-positive area in both groups (*n* = 3 per each time point). Error bar indicates s.d. **P* < 0.01. (d) The location of GFAP⁺EGFP⁺ reactive astrocytes shifted toward the lesion epicenter from 1 to 2 weeks in wild-type (WT) littermates, whereas their position remained relatively unchanged in *Nes-Stat3⁻/⁻* mice. Scale bar, 300 µm. (e) In *Nes-Stat3⁻/⁻* mice, Cre-mediated EGFP⁺ cells (green) were colocalized with GFAP⁺ reactive astrocytes (blue; arrows), but colocalization with phosphorylated Stat3 (red) was hardly observed at 4 d after injury. Scale bar, 100 µm. (f) Time course of functional recovery of lower limbs and the score of each mouse at 6 weeks after SCI. Whereas gradual recovery was observed in the subacute phase in wild-type (WT) littermates, little improvement was observed in *Nes-Stat3⁻/⁻* mice (*n* = 7 *Nes-Stat3⁻/⁻*; *n* = 8 wild-type). Data are mean ± s.e.m. **P* < 0.01, *★P* < 0.05.
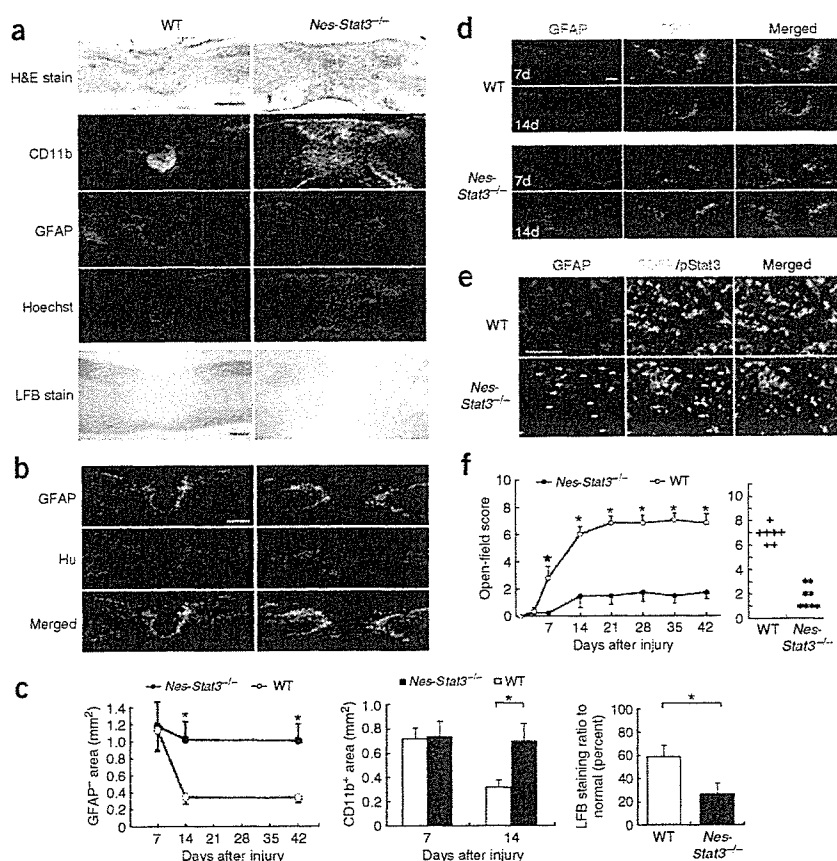
littermates and *Nes-Socs3⁻/⁻* mice became less pronounced at 2 weeks after injury, but *Nes-Socs3⁻/⁻* mice continually showed better motor function. Quantification of demyelination, oligodendrocyte-lost area and distal cord serotonergic innervation showed significant differences between the two groups (**Fig. 3f,h,i** and **Supplementary Fig. 4**). But GAP43⁺ regenerative fibers were comparable irrespective of genotype, and these fibers generally did not colocalize with 5HT⁺ fibers, indicating that the difference in serotonergic innervation did not result from regeneration (**Supplementary Fig. 5** online). These results suggest that the prompt contraction of the lesion spares more myelin, oligodendrocytes and serotonergic fibers, resulting in improved recovery.

Compared to wild-type mice, the development of reactive gliosis that secluded inflammatory cells was enhanced in *Nes-Socs3⁻/⁻* mice, whereas it was significantly delayed in *Nes-Stat3⁻/⁻* mice, indicating Stat3 signaling as an important factor in the developmental process of reactive gliosis after SCI (**Fig. 4a,b**).

Consistent with *in vivo* results, the *in vitro* migration behavior of astrocytes showed similar properties in a scratch-wounded assay that simulated the postinjury *in vivo* behavior of reactive astrocytes[17]. Astrocytes harvested from *Nes-Socs3⁻/⁻* mice showed a higher degree of migration, whereas impaired migration was observed in astrocytes of *Nes-Stat3⁻/⁻* compared to wild-type mice (**Fig. 4c–e**). As proliferation rates among the three groups were comparable, cell migration activity was not dependent upon cell proliferation activity (data not shown).

A recent report indicates a possible molecular link between Stat3-zinc signaling and cell movement[18]. The zinc transporter LIV1, identified as the transcriptional downstream target of Stat3, was found to be essential for the nuclear localization of the zinc-finger

protein Snail, a transcriptional repressor of the *Cdh1* gene (which encodes E-cadherin). Thus, the absence of Stat3 signaling causes dysregulation of cell adhesion and impairs cell movement. Strong support for this theory is given by the result that zinc deficiency impaired compaction of inflammatory cells by reactive astrocytes and increased the number of apoptotic cells after CNS injury[19]. In addition, CNS injury in knockout mice of metallothioneins (zinc-binding proteins involved in zinc ion regulation) had histological characteristics similar to *Nes-Stat3⁻/⁻* mice, such as impaired migratory behavior of reactive astrocytes, wide infiltration of inflammatory cells and severe impairment of wound healing[20]. On the other hand, astrocyte-targeted IL-6–expressing transgenic mice showed prompt migration of reactive astrocytes and compaction of inflammatory cells as well as substantial tissue repair after CNS injury[21] similar to *Nes-Socs3⁻/⁻* mice (though hyperactivation of IL-6 signaling without a specific cellular target caused considerably more damage owing to robust inflammation after CNS injury[6,22]). Here, expression of *Slc39a6* mRNA (encoding LIV1) in reactive astrocytes 5 d after injury was robust in wild-type mice but was limited in *Nes-Stat3⁻/⁻* mice. Consistent with *Slc39a6* mRNA expression, E-cadherin was expressed in reactive astrocytes of *Nes-Stat3⁻/⁻* but not in wild-type mice at 2 weeks after SCI. Furthermore, real-time RT-PCR of injured spinal cords showed differences in expression of *Scl39ac* mRNA among the three groups (**Fig. 4f–h**). These data provide insight into the mechanism of astrocytic migration through Stat3 signaling and indicate the significance of reactive astrocytes after CNS injury.

In our SCI model, the area of neuronal cell loss before the emergence of reactive astrocytes was comparable for wild-type and conditional knockout mice, suggesting that the effect of Stat3
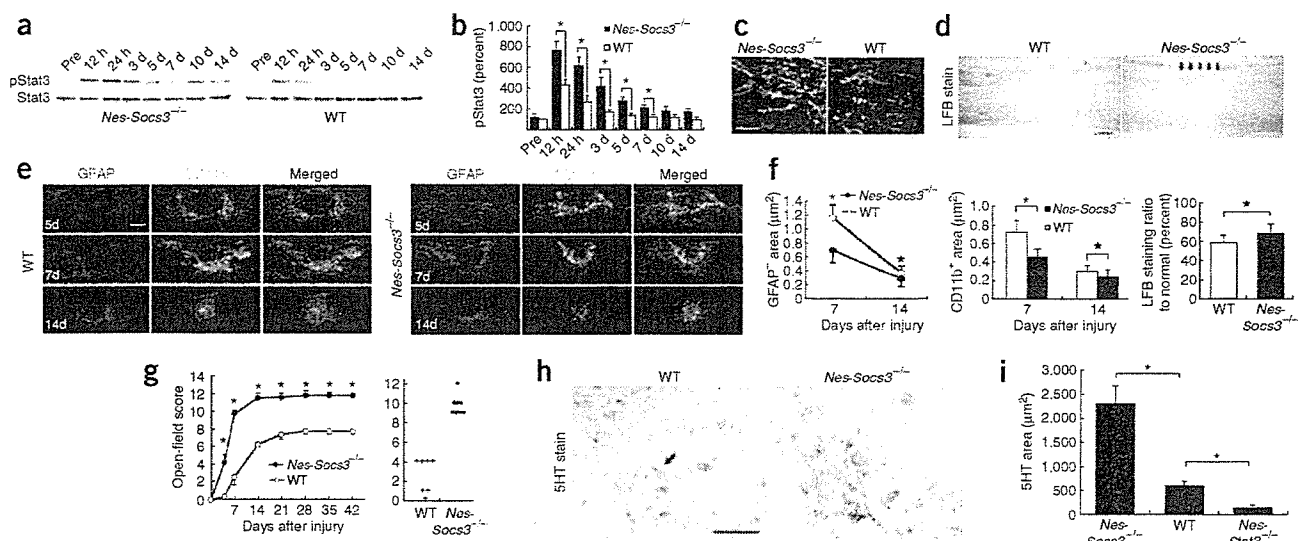
Figure 3 Enhanced activation of Stat3, prompt compaction of inflammatory cells and marked functional improvement in *Nes-Socs3*^{-/-} mice. (a) Western blot analysis of Stat3 phosphorylation in injured spinal cord of wild-type (WT) and *Nes-Socs3*^{-/-} mice. pStat3, phosphorylated Stat3. (b) Changes in the ratios of pStat3 to total Stat3 after SCI (mean ± s.e.m., n = 4 per group). *P < 0.05. (c) Immunostaining of pStat3 and reactive astrocytes at 7 d after SCI. GFAP, red; pStat3, green. Scale bar, 100 µm. (d) Luxol Fast Blue (LFB) staining in littermates and *Nes-Socs3*^{-/-} mice at 2 weeks after SCI. Arrows indicate the spared myelin in the dorsal part of the lesion epicenter. Scale bar, 300 µm. (e) Time course analysis of reactive astrocytes and CD11b^{+} cells. The early development of reactive astrocytes and compaction of inflammatory cells in *Nes-Socs3*^{-/-} mice was visible as early as 7 d after SCI. Scale bar, 500 µm. (f) Quantitative analysis of GFAP^{-} area, CD11b^{+} area and LFB-positive area (mean ± s.d., n = 4). *P < 0.01, *P < 0.05. (g) Time course of functional recovery and the score of each mouse at 7 d after SCI. Data are mean ± s.e.m. *P < 0.01. (h) 5HT staining of the ventral horn distal to the lesion in wild-type (WT) littermates and *Nes-Socs3*^{-/-} mice at 6 weeks after SCI. Arrow indicates spared 5HT[+] fibers. Scale bar, 100 µm. (i) Quantitative analysis of serotonergic innervation of the distal cord in the three groups (mean ± s.e.m., n = 4 per each group). *P < 0.01.

signaling on neuronal survival was minimal compared with its effect on the development and migration of reactive astrocytes (Supplementary Fig. 1).

The majority of studies on CNS injury have shown that the glial scar formed in part by reactive astrocytes hinders axonal regeneration. In mice lacking both GFAP and vimentin, reduced astroglial reactivity resulted in improved sprouting of axons and functional restoration after SCI[23]. But reactive astrocytes are also important for supporting repair of the blood-brain barrier. They prevent infiltration of CD45^{+} leukocytes and protect neurons and oligodendrocytes as shown by the selective ablation of dividing astrocytes using ganciclovir and GFAP-TK transgenic mice[24,25]. Here, we showed that Stat3 signaling in reactive astrocytes have a considerable role in the repair of injured tissue and the recovery of motor function. Although these results seem to conflict with one another, consideration of the timeframe in which these events were observed suggests a possible phase-dependent role of reactive astrocytes. In mice lacking both GFAP and vimentin, functional recovery was observed later than 2 weeks after injury[23], whereas substantial recovery was completed within 2 weeks after injury in *Nes-Stat3*^{-/-} and *Nes-Socs3*^{-/-} mice, suggesting that reactive astrocytes in the subacute phase repair tissue and restore function, whereas in the chronic phase of injury they impair axonal regeneration as a physical and chemical barrier.

Together, these results show that reactive astrocytes have a pivotal role in the repair of injured tissue and the recovery of motor function in the subacute phase after SCI, and that the function of reactive astrocytes is largely dependent on Stat3 signaling. This work also raises Stat3 signaling and reactive astrocytes as a potential new therapeutic target for the treatment of traumatic injury in CNS.

METHODS

Generation of conditional knockout mice. *Stat3*[loxP/loxP] mice, *Stat3*[loxP/-] mice, *Socs3*[loxP/loxP] mice, *Nes*-Cre mice and *CAG-CAT*[loxP/loxP]-EGFP transgenic mice were as described elsewhere[3,11,12,14,15,26]. To generate *Nes-Stat3*^{-/-} or *Nes-Socs3*^{-/-} mice, we crossed *Nes*-Cre mice with *Stat3*[loxP/loxP], *Stat3*[loxP/-] mice[3,26] or *Socs3*[loxP/loxP] mice[15]. We used wild-type littermates (*Stat3*[loxP/loxP] or *Socs3*[loxP/loxP]) as controls in histological and functional evaluations. We performed genotyping with primers described elsewhere[3,12,14,15]. All mice were housed in a temperature- and humidity-controlled environment on a 12-h light-dark cycle.

SCI model. We anesthetized adult C57BL/6J mice, wild-type littermates and conditional knockout mice (female, 8 weeks old) using an intraperitoneal injection of ketamine (100 mg/kg) and xylazine (10 mg/kg). After laminectomy at the tenth thoracic spinal vertebrae, we exposed the dorsal surface of the dura mater and induced SCI using a commercially available SCI device (60 kdyn using Infinite Horizon impactor, Precision Systems & Instrumentation) as previously described[27]. We evaluated motor function of the hind limbs with the locomotor rating test on the Basso-Beattie-Bresnahan (BBB) scale[28] for 6 weeks after injury. The obesity of *Nes-Stat3*^{-/-} mice was not a problem in this study, because their functional recovery was limited to the point at which weight bearing was not an issue. All procedures were approved by the ethics committee of Keio University and were in accordance with the Guide for the Care and Use of Laboratory Animals (US National Institutes of Health).

Immunohistochemistry. We anesthetized mice and transcardially perfused them with 4% paraformaldehyde in 0.1 M PBS. We removed spinal cords, embedded them in OCT compound and sectioned them sagittally at 20 µm on a cryostat. We stained tissue sections with primary antibodies to GFAP (DAKO), cleaved caspase-3 (Cell Signaling), CD11b (a marker of monocyte/macrophages and granulocytes; MBL), BrdU (Chemicon), Nestin (Rat 401, Chemicon), GFP (MBL), phosphorylated Stat3 (Cell Signaling), GSTπ (BD Biosciences), serotonin (5HT; DiaSorin, Inc.), GAP43 (Chemicon), E-cadherin
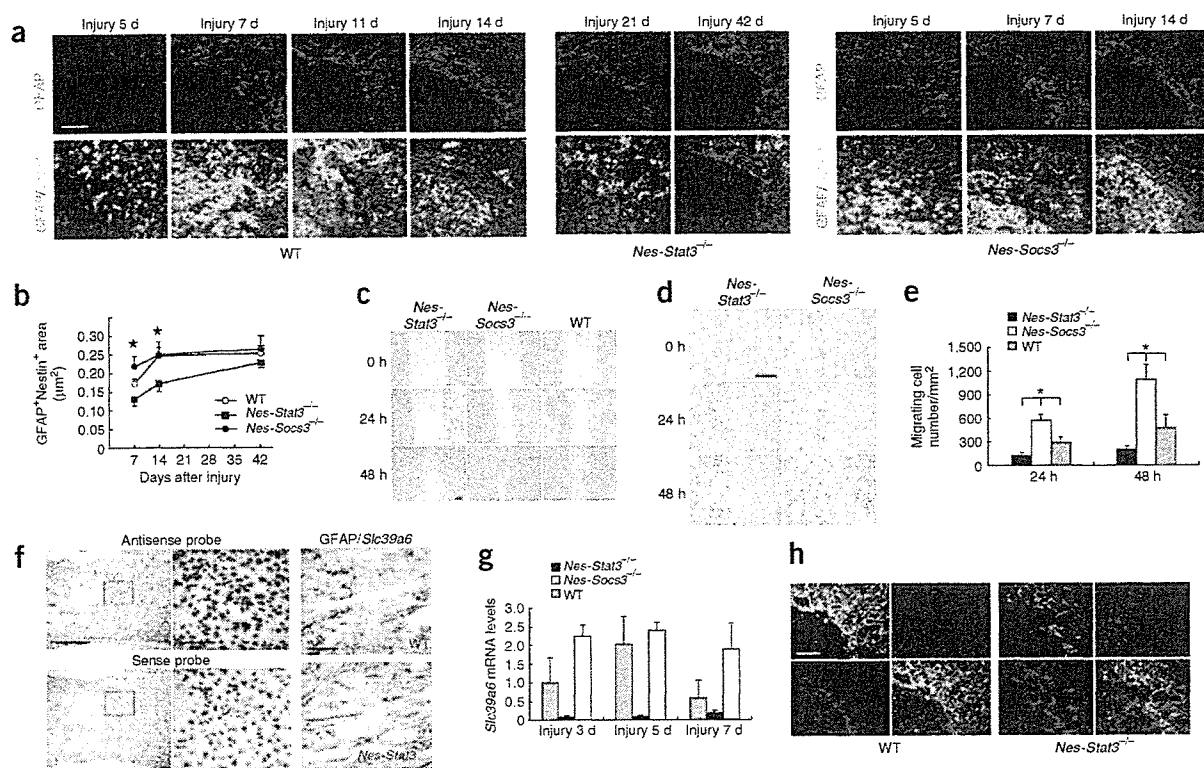
Figure 4 Involvement of Stat3 signaling in the development of reactive gliosis *in vivo*, the migration of reactive astrocytes *in vitro* and the transcriptional activity of LIV1. (a) Morphology of reactive astrocytes around the lesion area and infiltration of inflammatory cells in wild-type (WT), *Nes-Stat3^{-/-}* and *Nes-Socs3^{-/-}* mice. Scale bar, 100 μm. (b) The amount of reactive gliosis was measured as GFAP+Nestin+ (EGFP) area in the three groups (*n* = 3). Error bar indicates s.e.m. *P < 0.05. (c) *In vitro* scratch injury of monolayer cultured astrocytes derived from wild-type (WT), *Nes-Stat3^{-/-}* and *Nes-Socs3^{-/-}* mice. Scale bar, 20 μm. (d) Magnified image of reactive astrocytes derived from *Nes-Stat3^{-/-}* and *Nes-Socs3^{-/-}* mice. Scale bar, 20 μm. (e) Migrating cells were quantified as mean number ± s.e.m. per millimeter squared beyond the wound edge (*n* = 3). *P < 0.01. (f) *In situ* hybridization of *Slc39a6* mRNA in injured spinal cord. *Slc39a6* mRNA was observed in GFAP+ reactive astrocytes in wild-type but was rarely found in *Nes-Stat3^{-/-}* mice. Scale bars, 200 μm (upper left panel), 50 μm (upper middle panel) and 50 μm (upper right panel). (g) Expression of *Slc39a6* mRNA in injured spinal cords as determined by real-time RT-PCR in the three groups (*n* = 3). Each group was normalized to *Gapdh* values. There are significant differences (*P* < 0.01) among the three groups at each time point. Error bar indicates s.e.m. (h) Expression of E-cadherin (red) was not observed in reactive astrocytes of wild-type mice, whereas its active expression was observed in *Nes-Stat3^{-/-}* mice at 2 weeks after SCI. GFAP, green; Hoechst stain, blue. Scale bar, 100 μm.

(Santa Cruz) and Hu[29] (a gift from R. Darnell, The Rockefeller University). We performed nuclear counterstaining with Hoechst 33342 (Molecular Probes). Images were obtained by fluorescence microscopy (Axioskop 2 Plus; Carl Zeiss) or confocal microscopy (LSM510; Carl Zeiss). To quantify the immunopositive and immunonegative area *in vivo*, we selected five representative midsagittal sections in each mouse and measured the area with the MCID system (Imaging Research, Inc.). We quantified the immunopositive area using grain counting and detected the immunonegative area by quantifying the dark area after image binarization. For myelin staining, we performed Luxol Fast Blue (LFB) stain. For comparison of LFB positive area, we selected five representative sagittal sections (3 mm long) of injured spinal cords (2 weeks after SCI) from positions 0.25 mm and 0.5 mm right of the midline, at the midline, and 0.25 mm and 0.5 mm left of the midline and LFB-positive area (blue area), and measured them by MCID system (grain counting), and calculated the ratio to normal section. To count GFAP+BrdU+ cells, we selected five representative sagittal sections and randomly captured six regions in each section at ×200 magnification by confocal microscopy. For quantification of 5HT+ fibers, we randomly captured ten regions in each axial section of distal cord at ×200 magnification, and we quantified the total 5HT+ area using the MCID system. We maintained light intensity and threshold values at constant levels for all analyses. In all sagittal sections shown here, the left side is rostral.

In vitro **migration assay.** We prepared primary astrocytes from 2-d-old wild-type and conditional knockout mice as previously described[30]. After several passages in DMEM with 10% FBS, we trypsinized cells and plated them to confluency on coverslips coated with poly-L-lysine. After reaching subconfluency, we treated cells with 10 μg/ml mitomycin C for 2 h to avoid the effects of cell proliferation and then subjected them to scratching. We created a cell-free area by scratching the monolayer with a pipette tip and evaluated the migration of cells to the cell-free area from the surrounding area at 24 h and 48 h. We counted the number of migrating astrocytes after taking photographs of ten nonoverlapping fields.

Western blotting. We anesthetized SCI mice, transcardially perfused them with saline, and isolated and lysed a 4-mm long section of the injured spinal cord. We resolved lysates with SDS-PAGE and immunoblotted membranes with antibody to phosphorylated Stat3 (Tyr705) and antibody to Stat3 (Cell Signaling).

In situ **hybridization.** For detection of *Slc39a6* mRNA, we subcloned a 774-bp DNA fragment corresponding to the nucleotide positions 331–1104 of mouse *Slc39a6* into pGEMT-Easy vector (Promega) and used it to generate sense or antisense RNA probes. We hybridized paraffin-embedded spinal cord sections (6 μm) with digoxigenin-labeled RNA probes at 60 °C for 16 h. We detected the bound label using NBT-BCIP, an alkaline phosphate color substrate. We counterstained sections with Kernechtrot.

Real-time quantitative PCR. We isolated total RNA from the injured spinal cord (4 mm long) using the RNeasy Kit (Qiagen) and obtained cDNA by

LETTERS

reverse transcriptase reaction. For quantitative analysis of *Slc39a6* mRNA expression, we used the cDNA as a template in a TaqMan real-time PCR assay using the ABI Prism 7000 sequence detection system (Applied Biosystems) according to the manufacturer's protocol. We performed the amplification using the following primers: forward primer, 5'-TGAAGGCAGCACCAATAG CA-3'; reverse primer, 5'-GGCCTGGATGGTGATCATG-3'; and TaqMan probe, 5'-FAM-CGTCACTGAAATTGTGCAGCCCGTC-TAMRA-3'.

Statistical analysis. We performed statistical analysis with an unpaired two-tailed Student *t*-test for single comparisons, and ANOVA followed by the Tukey-Kramer test for multiple comparisons. For the open-field score, we used repeated-measures ANOVA and the Mann-Whitney *U*-test. In all statistical analyses, significance was accepted at $P < 0.05$.

Accession codes. GenBank: *Mus musculus* solute carrier family 39 (metal ion transporter) number 6 (Slc39a6), NM_139143.

Note: Supplementary information is available on the Nature Medicine website.

1. Silver, J. & Miller, J.H. Regeneration beyond the glial scar. *Nat. Rev. Neurosci.* **5**, 146–156 (2004).
2. Wang, T. *et al.* Regulation of the innate and adaptive immune responses by Stat-3 signaling in tumor cells. *Nat. Med.* **10**, 48–54 (2004).
3. Sano, S. *et al.* Keratinocyte-specific ablation of Stat3 exhibits impaired skin remodeling, but does not affect skin morphogenesis. *EMBO J.* **18**, 4657–4668 (1999).
4. Hirano, T., Ishihara, K. & Hibi, M. Roles of STAT3 in mediating the cell growth, differentiation and survival signals relayed through the IL-6 family of cytokine receptors. *Oncogene* **19**, 2548–2556 (2000).
5. Sriram, K., Benkovic, S.A., Hebert, M.A., Miller, D.B. & O'Callaghan, J.P. Induction of gp130-related cytokines and activation of JAK2/STAT3 pathway in astrocytes precedes up-regulation of glial fibrillary acidic protein in the 1-methyl-4-phenyl-1,2,3,6-tetrahydropyridine model of neurodegeneration: key signaling pathway for astrogliosis *in vivo? J. Biol. Chem.* **279**, 19936–19947 (2004).
6. Kerr, B.J. & Patterson, P.H. Potent pro-inflammatory actions of leukemia inhibitory factor in the spinal cord of the adult mouse. *Exp. Neurol.* **188**, 391–407 (2004).
7. Xia, X.G., Hofmann, H.D., Deller, T. & Kirsch, M. Induction of STAT3 signaling in activated astrocytes and sprouting septal neurons following entorhinal cortex lesion in adult rats. *Mol. Cell. Neurosci.* **21**, 379–392 (2002).
8. Klein, M.A. *et al.* Impaired neuroglial activation in interleukin-6 deficient mice. *Glia* **19**, 227–233 (1997).
9. Frisen, J., Johansson, C.B., Torok, C., Risling, M. & Lendahl, U. Rapid, widespread, and longlasting induction of nestin contributes to the generation of glial scar tissue after CNS injury. *J. Cell Biol.* **131**, 453–464 (1995).
10. Johansson, C.B., Lothian, C., Molin, M., Okano, H. & Lendahl, U. Nestin enhancer requirements for expression in normal and injured adult CNS. *J. Neurosci. Res.* **69**, 784–794 (2002).
11. Takeda, K. *et al.* Stat3 activation is responsible for IL-6-dependent T cell proliferation through preventing apoptosis: generation and characterization of T cell-specific Stat3-deficient mice. *J. Immunol.* **161**, 4652–4660 (1998).
12. Betz, U.A., Vosshenrich, C.A., Rajewsky, K. & Muller, W. Bypass of lethality with mosaic mice generated by Cre-loxP-mediated recombination. *Curr. Biol.* **6**, 1307–1316 (1996).
13. Gao, Q. *et al.* Disruption of neural signal transducer and activator of transcription 3 causes obesity, diabetes, infertility, and thermal dysregulation. *Proc. Natl. Acad. Sci. USA* **101**, 4661–4666 (2004).
14. Kawamoto, S. *et al.* A novel reporter mouse strain that expresses enhanced green fluorescent protein upon Cre-mediated recombination. *FEBS Lett.* **470**, 263–268 (2000).
15. Mori, H. *et al.* Socs3 deficiency in the brain elevates leptin sensitivity and confers resistance to diet-induced obesity. *Nat. Med.* **10**, 739–743 (2004).
16. Kubo, M., Hanada, T. & Yoshimura, A. Suppressors of cytokine signaling and immunity. *Nat. Immunol.* **4**, 1169–1176 (2003).
17. Faber-Elman, A., Solomon, A., Abraham, J.A., Marikovsky, M. & Schwartz, M. Involvement of wound-associated factors in rat brain astrocyte migratory response to axonal injury: *in vitro* simulation. *J. Clin. Invest.* **97**, 162–171 (1996).
18. Yamashita, S. *et al.* Zinc transporter LIVI controls epithelial-mesenchymal transition in zebrafish gastrula organizer. *Nature* **429**, 298–302 (2004).
19. Penkowa, M., Giralt, M., Thomsen, P.S., Carrasco, J. & Hidalgo, J. Zinc or copper deficiency-induced impaired inflammatory response to brain trauma may be caused by the concomitant metallothionein changes. *J. Neurotrauma* **18**, 447–463 (2001).
20. Penkowa, M., Carrasco, J., Giralt, M., Moos, T. & Hidalgo, J. CNS wound healing is severely depressed in metallothionein I- and II-deficient mice. *J. Neurosci.* **19**, 2535–2545 (1999).
21. Penkowa, M. *et al.* Astrocyte-targeted expression of IL-6 protects the CNS against a focal brain injury. *Exp. Neurol.* **181**, 130–148 (2003).
22. Lacroix, S., Chang, L., Rose-John, S. & Tuszynski, M.H. Delivery of hyper-interleukin-6 to the injured spinal cord increases neutrophil and macrophage infiltration and inhibits axonal growth. *J. Comp. Neurol.* **454**, 213–228 (2002).
23. Menet, V., Prieto, M., Privat, A. & Gimenezy Ribotta, M. Axonal plasticity and functional recovery after spinal cord injury in mice deficient in both glial fibrillary acidic protein and vimentin genes. *Proc. Natl. Acad. Sci. USA* **100**, 8999–9004 (2003).
24. Bush, T.G. *et al.* Leukocyte infiltration, neuronal degeneration, and neurite outgrowth after ablation of scar-forming, reactive astrocytes in adult transgenic mice. *Neuron* **23**, 297–308 (1999).
25. Faulkner, J.R. *et al.* Reactive astrocytes protect tissue and preserve function after spinal cord injury. *J. Neurosci.* **24**, 2143–2155 (2004).
26. Ozawa, Y. *et al.* Downregulation of STAT3 activation is required for presumptive rod photoreceptor cells to differentiate in the postnatal retina. *Mol. Cell. Neurosci.* **26**, 258–270 (2004).
27. Scheff, S.W., Rabchevsky, A.G., Fugaccia, I., Main, J.A. & Lumpp, J.E., Jr. Experimental modeling of spinal cord injury: characterization of a force-defined injury device. *J. Neurotrauma* **20**, 179–193 (2003).
28. Basso, D.M., Beattie, M.S. & Bresnahan, J.C. Graded histological and locomotor outcomes after spinal cord contusion using the NYU weight-drop device versus transection. *Exp. Neurol.* **139**, 244–256 (1996).
29. Okano, H.J. & Darnell, R.B. A hierarchy of Hu RNA binding proteins in developing and adult neurons. *J. Neurosci.* **17**, 3024–3037 (1997).
30. Sanai, N. *et al.* Unique astrocyte ribbon in adult human brain contains neural stem cells but lacks chain migration. *Nature* **427**, 740–744 (2004).

Wnt Signaling and a Hox Protein Cooperatively Regulate PSA-3/Meis to Determine Daughter Cell Fate after Asymmetric Cell Division in *C. elegans*

Yukinobu Arata,[1] Hiroko Kouike,[2,3,4,8]
Yanping Zhang,[5,9] Michael A. Herman,[5]
Hideyuki Okano,[2,3,4] and Hitoshi Sawa[1,4,6,7,*]
[1] Laboratory for Cell Fate Decision
RIKEN
Center for Developmental Biology
Kobe 650-0047
Japan
[2] Core Research for Evolutional Science and Technology
Japan Science and Technology Corporation
Saitama 332-0012
Japan
[3] Department of Physiology
Keio University School of Medicine
Tokyo 160-8582
Japan
[4] Division of Neuroanatomy
Osaka University Graduate School of Medicine
Osaka 565-0871
Japan
[5] Program in Molecular, Cellular, and Developmental
 Biology
Division of Biology
Kansas State University
Manhattan, Kansas 66506
[6] Division of Bioinformation
Department of Biosystems Science
Graduate School of Science and Technology
Kobe University
Kobe 650-0017
Japan
[7] Precursory Research for Embryonic Science and
 Technology
Japan Science and Technology Corporation
Saitama 332-0012
Japan

Summary

Asymmetric cell division is a mechanism for achieving cellular diversity. In *C. elegans*, many asymmetric cell divisions are controlled by the Wnt-MAPK pathway through POP-1/TCF. It is poorly understood, however, how POP-1 determines the specific fates of daughter cells. We found that *nob-1*/Hox, *ceh-20*/Pbx, and a Meis-related gene, *psa-3*, are required for asymmetric division of the T hypodermal cell. *psa-3* expression was asymmetric between the T cell daughters, and it was regulated by POP-1 through a POP-1 binding site in the *psa-3* gene. *psa-3* expression was also regulated by NOB-1 and CEH-20 through a NOB-1 binding sequence in a *psa-3* intron. PSA-3 can bind CEH-20 and function after the T cell division to promote the proper fate of the daughter cell. These results indicate that cooperation between Wnt signaling and a Hox protein functions to determine the specific fate of a daughter cell.

*Correspondence: sawa@cdb.riken.jp
[8] Present address: Laboratory of Auditory Disorders, National Institute of Sensory Organs, National Hospital Organization, Tokyo Medical Center, Tokyo 152-8902, Japan.
[9] Present address: Department of Molecular and Microbiology, UF Shands Cancer Center, College of Medicine, University of Florida, Gainesville, Florida 32610.

Introduction

During animal development, a zygote generates diverse cell types that have different temporal and spatial identities; asymmetric cell division is a fundamental mechanism for generating this diversity. In *Drosophila*, the asymmetric divisions of a number of neuroblasts are regulated by the asymmetric segregation of the Numb and Prospero proteins (Jan and Jan, 2001). In *C. elegans*, as described below, many asymmetric divisions are regulated by the Wnt-MAPK pathway. Although the respective mechanisms in each of these organisms are used repeatedly during development, the fates of the daughter cells are distinct and depend on their position in the animal's body. In *Drosophila*, segmentation genes determine the specificities of neuroblast and postmitotic neurons (Bhat, 1999), and, in *C. elegans*, a *Hox* gene, *mab-5*, is involved in cell fate specification after the asymmetric division (Salser and Kenyon, 1996). Therefore, these genes, which regulate positional identity, are likely to be important for determining specificities of cell fates after asymmetric division.

In *C. elegans*, many asymmetric divisions in embryonic and postembryonic development are regulated by the Wnt-MAPK signaling pathway (Herman, 2002; Thorpe et al., 2000). This pathway regulates the asymmetric nuclear localization of the POP-1/TCF transcription factor between daughter cells (POP-1 asymmetry). POP-1 asymmetry is suggested to create distinct POP-1 transcriptional activities in each daughter cell (Kidd et al., 2005; Shetty et al., 2005). POP-1 asymmetry is observed in most cell divisions along the anteroposterior axis (Herman, 2001; Lin et al., 1998). In addition, LIT-1/NLK, a MAP kinase that regulates POP-1 asymmetry, is required for many embryonic and postembryonic divisions (Kaletta et al., 1997; Takeshita and Sawa, 2005). Taken together, these findings indicate that POP-1 functions as a universal factor to determine asymmetry between daughter cells throughout *C. elegans* development. However, in spite of this common mechanism for asymmetric division, the daughter cells have unique cell fates. Therefore, how POP-1 cooperates with genes that regulate positional identity is a critical issue.

Six *Hox* genes are encoded in a loosely linked cluster in *C. elegans*: *ceh-13*, *lin-39*, *mab-5*, *egl-5*, *php-3*, and *nob-1* (Kenyon et al., 1997; Van Auken et al., 2000). Of these, *lin-39*, *mab-5*, and *egl-5* are expressed in a position-specific manner and regulate cell identities (Kenyon et al., 1997). *nob-1* mutants show abnormal tail morphogenesis and the anterior transformation of posterior gut and neural cells, suggesting that *nob-1* regulates positional identity in the posterior region (Van Auken et al., 2000). In many organisms, members of the Pbx and

Meis protein families help the Hox proteins select the correct DNA binding site and regulate their transactivation activity as their cofactors (Mann and Affolter, 1998). The nuclear localization of the Pbx proteins is regulated by their binding with Meis proteins (Affolter et al., 1999). In *C. elegans*, the CEH-20 protein also functions cooperatively with the LIN-39 protein on the promoter of the *hlh-8* and *egl-18* genes to regulate their expression (Koh et al., 2002; Liu and Fire, 2000), suggesting that Hox proteins and their cofactors cooperatively determine spatial specificities in *C. elegans*.

Seam cells, on the lateral sides of the animals, divide asymmetrically in postembryonic development. Among the seam cells, asymmetric division of the T cell is regulated by the Wnt-MAPK signaling pathway, including LIN-44/Wnt, LIN-17/Frizzled, LIT-1, WRM-1/β-catenin, and POP-1 (Herman, 2002; Takeshita and Sawa, 2005). The T cell divides asymmetrically; thus, the anterior daughter (T.a) produces hypodermal cells, while the posterior daughter (T.p) generates neural cells, including the phasmid socket cells. In *pop-1* mutants, the T cell division is symmetric, and both T.a and T.p produce hypodermal cells (Herman, 2001), resulting in the absence of phasmid socket cells (Psa phenotype, for phasmid socket absent). Here, we show that *nob-1/*Hox *ceh-20/*Pbx and a novel Meis-related gene, *psa-3*, are required for the asymmetric T cell division. We found that *psa-3* is expressed asymmetrically between the T cell daughters and that the asymmetric *psa-3* expression is regulated by the Wnt-MAPK pathway as well as by NOB-1 and CEH-20. These findings indicate that two classes of genes, which discretely regulate asymmetric division and positional identity, specify the daughter fates in the asymmetric T cell division.

Results

*psa-3/*Meis, *ceh-20/*Pbx, and *nob-1/*Hox Are Required for the Asymmetric T Cell Division

We identified mutants of *psa-3(os8)*, *ceh-20*, and *nob-1* in a screen for mutants with the Psa phenotype (Sawa et al., 2000), and *psa-3(mh32)* and *psa-3(mh55)* in a screen for phasmid-defective mutants, by using the dye-filling assay (Zhao et al., 2002) (Table 1). The previously identified *ceh-20(ay38)* and *nob-1(ct230)* mutants (Van Auken et al., 2000, 2002) also show the Psa phenotype (Table 1). We determined the T cell lineage in these mutants. In *nob-1*, *ceh-20*, and *psa-3* mutants, the asymmetry of the divisions was often disrupted, leading to the production of hypodermal instead of neural cells by T.p (Figure 1; types II, III, and IV). Therefore, we concluded that these mutants were defective in the asymmetric T cell division. We also observed that the T cell did not divide during the L1 stage in some *nob-1* mutants (Figure 1; type V). In these animals, the nucleus of the T cell was smaller than in wild-type, although the morphology of the nucleus was hypodermal (data not shown), suggesting that the T cell lost its identity in some of the *nob-1* mutants. Such abnormal morphology of the T cell was not observed in other *nob-1* animals or in *ceh-20* or *psa-3* animals.

In *Drosophila* neuroblasts, the Hox genes *abd-A and Abd-B* repress the establishment of cell polarity before division, resulting in the symmetric division of a neuro-

Table 1. *psa-3*, *ceh-20*, and *nob-1* Are Required for Asymmetric T Cell Division

Genotype	% Psa (n)
N2	0% (162)
psa-3(os8)	38.5% (156)
psa-3(os8)[a]	40.0% (60)
psa-3(os8);osEx[pPS3.16]	4.5% (110)
psa-3(os8);unc-76;osEx[hsp::PSA-3][a]	3.1% (126)
psa-3(os8);unc-76;osEx[hsp::PSA-3::GFP][a]	4.5% (110)
psa-3(RNAi)	7.0% (242)
psa-3(mh32)	45.8% (120)
psa-3(mh55);him-5	26.9% (120)
psa-3(tm656)	0% (102)
psa-3(tm657)	3.9% (178)
psa-3(os8);unc-76;osEx[psa-3::gfp]	2.8% (176)
psa-3(os8);unc-76;osEx[mut-psa-3::gfp]	38.6% (140)
ceh-20(os39)	77.0% (122)
ceh-20(ay38)unc-36(e251)	50.0% (172)
ceh-20(os39);osEx[ceh-20::gfp]	16.1% (112)
ceh-20(os114)unc-119(e2498)	50.8% (122)
nob-1(os6)	37.7% (122)
nob-1(ct230)	35.5% (138)
nob-1(os6);unc-76;osEx[hsp::PSA-3][a]	42.8% (112)
php-3(ok919)	12.1% (182)

[a] Results after the heat shock treatment.

blast (Berger et al., 2005). Therefore, we examined whether *nob-1* regulates the cell polarity in the T cell division. However, the asymmetric nuclear localization of POP-1 between the T cell daughters (POP-1 asymmetry) was not affected in *nob-1* mutants (normal in 26/27 *nob-1* mutants, and in 23/24 wild-type animals), indicating that *nob-1* is unlikely to be involved in cell polarity in the asymmetric T cell division.

psa-3 Encodes a Meis-Related Protein

The *psa-3* gene was genetically mapped between *unc-7* and *lin-15* on the right arm of the X chromosome (see Experimental Procedures). A cosmid, F39D8, in this region and its subclone, pPS3.11, rescued the Psa phenotype of *psa-3* mutants (Figure 2A; data not shown). In the region covered by pPS3.11, two genes are predicted in the *C. elegans* database (WormBase): *F39D8.2* and *pqn-36 (F39D8.1)*. The *pqn-36* gene is located in an intron of the *F39D8.2* gene in the inverted orientation (Figure 2A). To determine which of these predicted genes is *psa-3*, we constructed a plasmid (pPS3.16) that contained the entire *F39D8.2* gene but lacked most of the *pqn-36* gene, except its C terminus. pPS3.16 efficiently rescued the Psa phenotype of the *psa-3* mutants (Figure 2A; Table 1). To confirm that the *psa-3* gene is *F39D8.2*, we
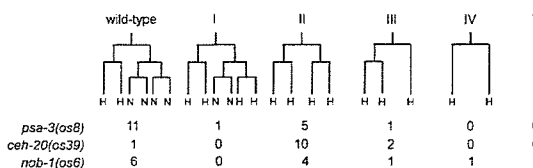

Figure 1. Abnormal T Cell Lineages in *psa-3*, *nob-1*, and *ceh-20* Mutants at the L1 Stage

H or N indicates a hypodermal or neural cell, respectively, judged by the morphology of the nucleus (Sawa et al., 2000). The numbers of T cells that showed the lineages are indicated below the diagrams.
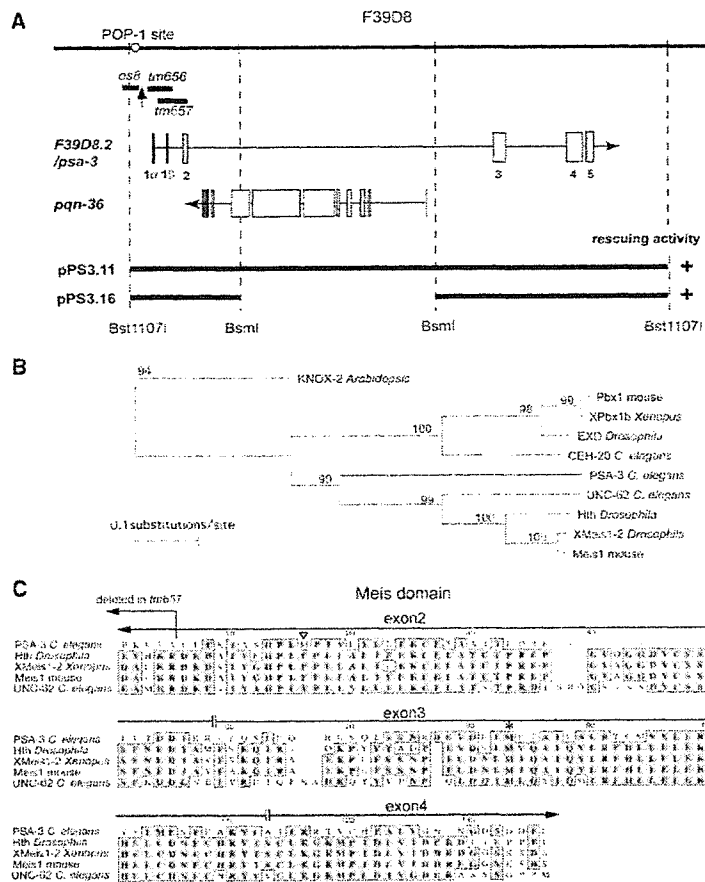
A

B

C

Figure 2. *psa-3* Encodes a Meis-Related Protein

(A) Schematic representation of the *psa-3* locus. Exons are indicated by open boxes. 5' of the *F39D8.2* gene is on the left. The *pqn-36* gene is oriented inversely to the *F39D8.2* gene. The deletions in *os8*, *tm656*, and *tm657* are indicated by horizontal bars, and the point mutation in *os8* is indicated by an upward arrow. The POP-1 binding sequence is indicated by an open circle. Regions covered by the *psa-3* rescuing plasmids are indicated at the bottom.

(B) A phylogenetic tree of the Meis and PBC domains was constructed with the neighbor-joining method (Saitou and Nei, 1987) by using 153 amino acid sites. KNOX-2 in *Arabidopsis thaliana* was used as an outgroup. Bootstrap analysis was performed with 1000 replicates.

(C) Alignment of the Meis domains. An open triangle and an asterisk indicate putative initiation methionine residues from the *psa-3* transcripts that start with SL1-exon2 and SL1-exon3, respectively. The region deleted in *tm657* is indicated.

expressed a cDNA (containing exon 1β, see below) under the control of a heat shock promoter and found that the Psa phenotype of the *psa-3* mutants was efficiently rescued (Table 1). In addition, RNAi of the *F39D8.2* gene caused the Psa phenotype (Table 1). Taking these findings together, we concluded that *F39D8.2* is the *psa-3* gene.

The predicted PSA-3 protein has a domain homologous to the Meis domain (Figures 2B and 2C), but it does not have a homeobox, both of which are conserved among the previously known Meis-family transcription factors (Burglin, 1997; Mann and Affolter, 1998). By sequencing *psa-3* cDNAs, we found two alternative first exons (exon1α and exon1β). In addition, we detected transcripts in which the SL1 *trans*-spliced leader directly connected to exon2 or exon3 (Figure 2A). Of these, the SL1-exon1α and SL1-exon1β transcripts were predicted to produce proteins with an intact Meis domain. By using the first ATG in the exon as a start codon, the SL1-exon2 and SL1-exon3 transcripts were predicted to produce proteins that lacked the initial 15 amino acids and about half of the Meis domain, respectively (Figure 2C; open triangle and asterisk).

To identify the lesions in the *psa-3* gene locus, we sequenced the *psa-3* gene in the *psa-3* mutants. *os8* did not have mutations in the coding region; instead, it had a 259 bp deletion and a point mutation upstream of exon1α (Figure 2A; Experimental Procedures). The

deletion included the sequence (CTTTTGATG) to which the POP-1 protein is known to bind directly (Streit et al., 2002). PCR and Southern blot analyses indicated that *mh32* and *mh55* had DNA rearrangements in the promoter region of the *psa-3* gene (data not shown), although we did not determine the exact nature of their mutations. We also analyzed *tm656* and *tm657*, which were isolated in a PCR-based screen for deletion mutants (National BioResource Project). They had deletions in the coding region (Figure 2A; Experimental Procedures). *tm657*, but not *tm656*, exhibited the Psa phenotype, albeit weakly (Table 1). In *tm657*, all of exon1β and part of exon2 were deleted (Figures 2A and 2C), while in *tm656*, all of exon1α and exon1β were deleted, but none of exon2, which includes the region encoding the Meis domain (Figure 2A). Therefore, *tm656* probably lacked the Psa phenotype because it produced functional *psa-3* transcripts that started from SL1-exon2.

The *psa-3*/Meis Expression Is Regulated by POP-1/TCF

As described above, *psa-3(os8)* had a deletion of the putative POP-1 binding sequence, raising the possibility that *psa-3* is a target gene of POP-1. To examine this possibility, we analyzed *psa-3* expression by using a *gfp* fusion construct containing the *psa-3* promoter and the entire coding region. This construct rescued
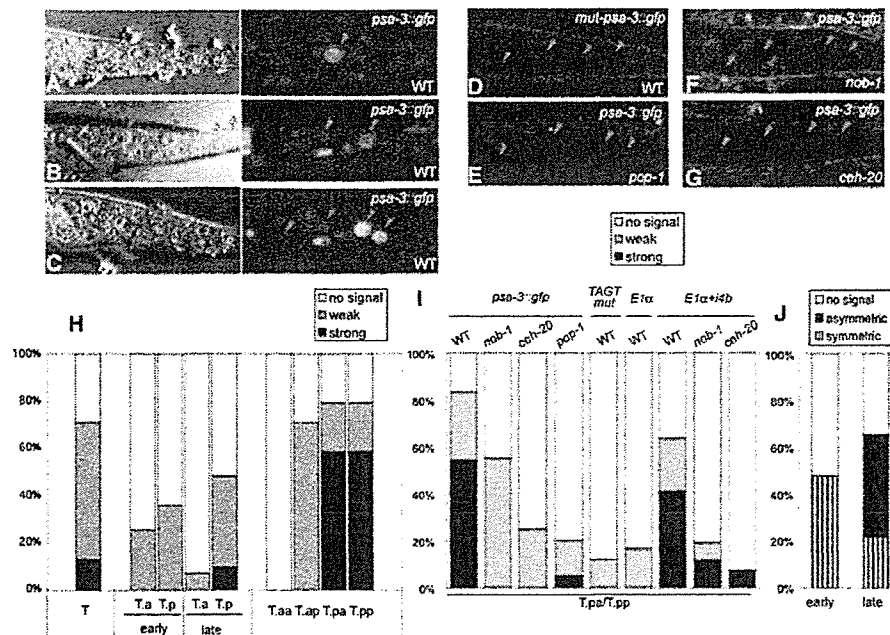
Figure 3. *psa-3* Expression Is Regulated by *pop-1*, *nob-1*, and *ceh-20*

(A–C) The expression of *psa-3::gfp* in the (A) T cell, (B) its daughters, and (C) its granddaughters in wild-type. Arrowheads indicate the nucleus of the T cell and its descendants. Anterior is to the left, and ventral is to the bottom.

(D–G) *psa-3* expression in the granddaughters of the T cell was examined, by using either (D) *mut-psa-3::gfp* with an altered POP-1 binding site in wild-type or (E) *psa-3::gfp* in *pop-1(q645)*, (F) *nob-1(os6)*, or (G) *ceh-20(os39)* mutants.

(H–J) The intensity of *psa-3::gfp* was examined in the T cell or its progeny. In each experiment, more than 20 samples were scored. "Early" and "late" indicate before and after the V6 cell division, respectively, which occurs ~30 min after the T cell division. The signal intensity representing "strong expression" (black bars) or "weak expression" (gray bars) was more or less than five times higher than background (no signal, open bars), respectively. (H) *psa-3* expression in T cells, daughter cells, or granddaughter cells in wild-type. (I) Expression of the indicated *psa-3::gfp* fusion constructs (see Figure 4A) in the posterior granddaughter cells (T.pa or T.pp) was examined in wild-type (WT), or *nob-1(os6)*, *ceh-20(os39)*, or *pop-1(q645)* mutants. (J) Animals that showed asymmetric or symmetric *psa-3* expression in the daughter cells were scored. "Asymmetric" (black bars) and "symmetric" (vertical hatched bars) mean that the intensities were higher in T.p than in T.a and equal between T.a and T.p, respectively.

the Psa phenotype of the *psa-3* mutants (Table 1). *psa-3* was expressed in the T cell, head neurons, posterior gut cells, hypodermal cells (hyp7, hyp9, and hyp10), and P blast cells (Figure 3A; data not shown). Of the seam cells, only the T cell expressed *psa-3* (data not shown). During mitosis of the T cell, the PSA-3 protein was uniformly distributed in the T cell (data not shown). Soon after the T cell division (before V6 cell division, which occurs about 30 min after T cell division), the *psa-3* expression in the two daughter cells was almost the same (Figures 3H and 3J; the early stage). In the later stage, after V6 cell division, the *psa-3* expression in T.a had decreased and that in T.p increased (Figures 3B, 3H, and 3J; the late stage). After the next round of divisions, the *psa-3* expression had greatly increased in the posterior (T.pa and T.pp), but not the anterior, granddaughters (Figures 3C and 3H). These data suggest that *psa-3* expression was induced in T.p after the T cell division, and that it accumulated in the posterior granddaughters.

To analyze the role of the putative POP-1 binding site in the promoter, we made a mutant *psa-3::gfp* construct (*mut-psa-3::gfp*) that had specific nucleotide substitutions within the POP-1 binding sequence (CT̲T̲T̲TGATG to CTG̲G̲A̲GATG; mutated nucleotides are underlined)

that were shown previously to disrupt POP-1 binding (Streit et al., 2002). We found that the *psa-3* expression and the rescuing activity were lost in the *mut-psa-3::gfp* construct (Figure 3D; Table 1). In addition, *psa-3* expression in the T.p lineage was much lower in a *pop-1* hypomorphic allele, *q645* (Figures 3E and 3I). POP-1 function is known to be required in T.p to determine the neural fate (Herman, 2001). Therefore, we concluded that POP-1 regulates *psa-3* expression in T.p through the POP-1 binding site.

We further examined the *psa-3* expression in *lin-44/* Wnt or *lin-17*/Frizzled mutants (see Table S1 in the Supplemental Data available with this article online). In wild-type, the *psa-3* expression was higher in T.p than in T.a. in most animals in which expression was detected (T.a < T.p in Table S1). In contrast, most *lin-44* or *lin-17* mutants did not show this expression pattern, but instead showed a symmetric or reversed pattern (T.a = T.p or T.a > T.p in Table S1). The defective *psa-3* expression in *lin-44* or *lin-17* mutants was consistent with the previous observation that the cell fates of T.a and T.p are frequently reversed or symmetric in *lin-44* or *lin-17* mutants (Herman, 2002). Taking these findings together, we concluded that *psa-3* is a target gene of the Wnt signaling pathway.

NOB-1/Hox and CEH-20/Pbx Are Positive Regulators of psa-3/Meis Expression

After the seam cell divisions, an asymmetric nuclear localization of POP-1 (POP-1 asymmetry) is observed in all of the daughter cells (Herman, 2001; Lin et al., 1998), and the asymmetric division of all seam cells is regulated, at least, by lit-1 and mom-4, which are upstream regulators of POP-1 in the Wnt-MAPK pathway (Takeshita and Sawa, 2005). Therefore, POP-1 is likely to regulate the asymmetric division of all seam cells. However, we showed that psa-3, a target gene of POP-1, is specifically expressed in the T cell and its descendants among the seam cells. To examine the possibility that the T cell-specific psa-3 expression is regulated by a Hox gene and its cofactor, we analyzed the expression of psa-3 in nob-1 and ceh-20 mutants. In these mutants, psa-3 expression was decreased in the T.p lineage (Figures 3F, 3G, and 3I). Therefore, NOB-1 and CEH-20 function as positive regulators of psa-3 expression. The psa-3 expression defect in nob-1 mutants was weaker than that in the ceh-20 or pop-1 mutants, suggesting that another posterior Hox gene, php-3, may function redundantly in the T cell lineage. Consistent with this, a php-3 deletion mutant also exhibited the Psa phenotype (Table 1).

Because NOB-1 and CEH-20 are transcription factors, they are likely to regulate the transcription of psa-3. However, among all of the seam cells, NOB-1 and CEH-20 might bind and stabilize PSA-3 in only the T cell. To examine this possibility, we transiently expressed the PSA-3::GFP fusion protein by using a heat shock promoter, and we examined its stability in the seam cells during the L1 stage. The level of the ectopically expressed PSA-3::GFP protein decreased at a similar rate in all of the seam cells (data not shown). Therefore, this result appears to indicate that the T cell-specific PSA-3::GFP expression among seam cells is not achieved by CEH-20 and NOB-1 stabilizing the PSA-3 protein.

NOB-1/Hox and CEH-20/Pbx Directly Regulate psa-3/Meis Expression through Intron4

To examine how NOB-1 and CEH-20 regulate psa-3 expression, we searched for regulatory elements in the psa-3 gene that were required for its expression by using a series of deletion constructs of psa-3::gfp (Figure 4A). The deletion constructs E1α, E2, E2-3, and E3 showed very weak expression, if any, in the T cell lineage, suggesting the presence of regulatory elements downstream of exon3. Deletion of intron4 (Δi4), but not intron3 (Δi3), also caused the loss of expression, indicating the presence of the regulatory elements in intron4. We further deleted parts of intron4 without affecting the splice sites (Δi4a and Δi4b). The gfp expression was decreased with the Δi4b construct, but not with Δi4a. With a smaller deletion (135 bp) in intron4 (Δi4c), the gfp expression was also decreased, indicating that this 135 bp region (the i4c region) was essential for psa-3 expression. To analyze the role of intron4 in more detail, we inserted the i4b region into the E1α construct downstream of the POP-1 binding site (E1α+i4b). This construct showed much stronger expression than the E1α construct (Figures 3I and 4A), confirming the presence of an enhancer element in the i4b region. In nob-1 or ceh-20 mutants carrying the E1α+i4b con-

struct, there was almost no gfp expression (Figure 3I), indicating that the element is responsible for the activity of NOB-1 and CEH-20. We concluded that NOB-1 and CEH-20 regulate psa-3 expression though an enhancer element in intron4.

To investigate whether NOB-1/Hox and CEH-20/Pbx directly regulate psa-3/Meis expression, we searched for binding sequences for CEH-20 (TGA[T or A]) (Liu and Fire, 2000) within the i4c region (a consensus binding sequence for NOB-1 has not been reported). We identified two candidate sites (Figure 4B; site1 and site2) and used Electrophoretic Mobility Shift Assays (EMSAs) to examine the ability of NOB-1 to bind them by using the indicated oligonucleotides (Figure 4B). Incubation of the H/P probe, which has the canonical binding sequence for the Hox-Pbx complex (Liu and Fire, 2000), with the hexahistidine-tagged NOB-1 protein (His-NOB-1) produced a single shifted band (Figure 4C, lanes 1–3). A similar shifted band was observed with the i4c-S2 probe (Figure 4C, lane 9), but not with the i4c-S1 probe (Figure 4C, lanes 4–6). The binding of NOB-1 to i4c-S2 was disrupted weakly by a mutation in the putative CEH-20 binding site (TGAT) and strongly by one in the adjacent TAGT sequence (i4c-S2 mut II and mut III, respectively; Figure 4C, lanes 12 and 13). Furthermore, the shifted band was competed out more efficiently by the cold i4c-S2 probe than by the i4c-S2 mut III probe (Figure 4C, lanes 17–19 and 20–22). Our results indicate that the NOB-1 protein specifically binds the TAGT sequence of the i4c-S2 probe.

We next examined the effects of CEH-20/Pbx on the NOB-1-DNA complexes. We found that the addition of GST fusion CEH-20 did not produce additional (supershifted) bands, but that it significantly increased the amount of NOB-1 complexed with the H/P or i4c-S2 probes (Figure 4D, lanes 1–4, 15–18; Figure 4E). Similar effects of CEH-20 were also observed even when the Pbx binding site was mutated in the H/P probe (Figure 4D, lanes 8–11; Figure 4E), suggesting that CEH-20 promotes the complex formation between NOB-1 and DNA independent of the CEH-20 binding site. This is consistent with previous reports that Abd-B-like Hox proteins, even in the presence of Pbx proteins, do not preferentially bind DNA containing the Pbx consensus site (Shen et al., 1997), and that NOB-1 belongs to the Abd-B family (Van Auken et al., 2000). The addition of an antibody against GST to a mixture of GST fusion CEH-20, His-NOB-1, and the DNA probes did not disrupt the complex formation or produce supershifted bands, while an antibody against NOB-1 disrupted the complex formation (Figure 4D, lanes 6–7, 13–14, and 20–21). These data suggest that CEH-20 does not form a stable complex with NOB-1 and DNA, at least in this assay system. One possible mechanism is that a transient protein-protein interaction between CEH-20 and NOB-1 (see below) induces a conformational change in NOB-1 that promotes its DNA binding ability. In any case, our results indicate that CEH-20 can facilitate NOB-1's binding to intron4 of the psa-3 gene.

To validate these results in vivo, we mutated the TAGT sequence in the psa-3::gfp construct as in the i4c-S2 mut III probe (Figure 4A; TAGT mut), and we found that the psa-3 expression from this construct was disrupted (Figures 3I and 4A). Therefore, the NOB-1 binding
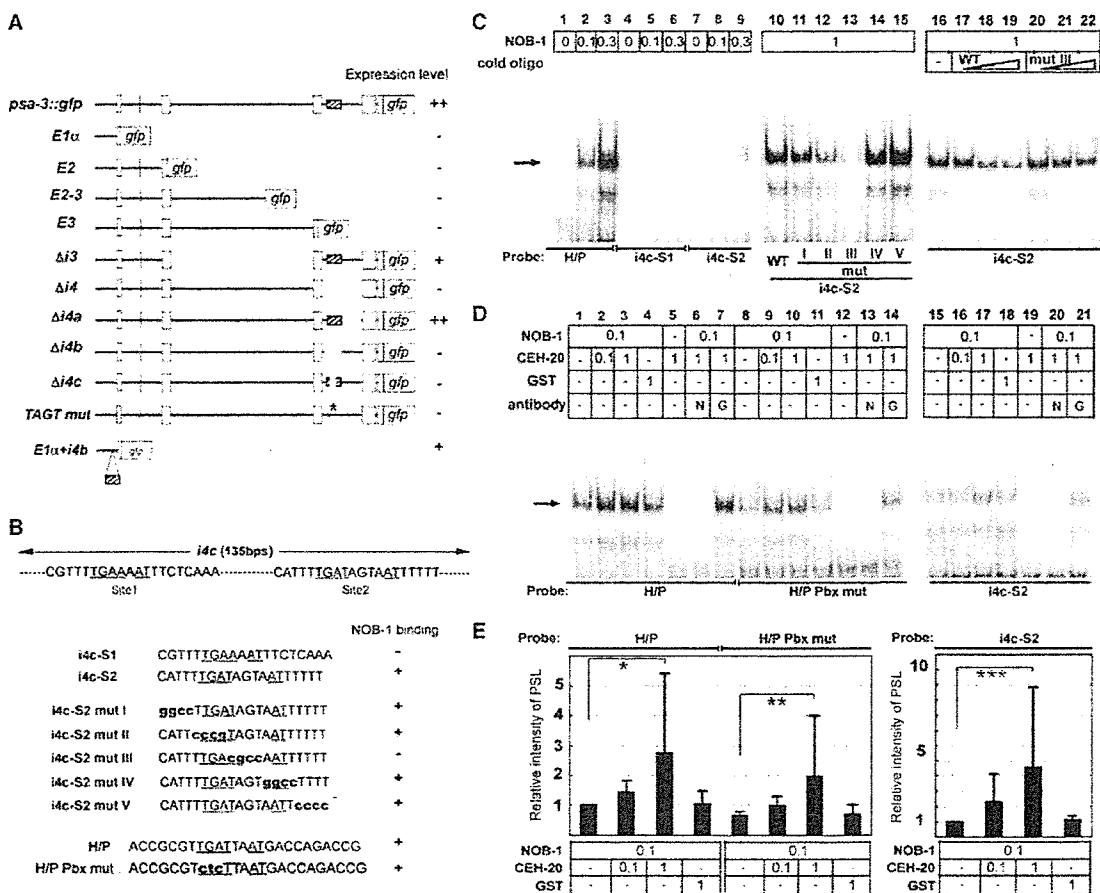
Figure 4. NOB-1 and CEH-20 Regulate *psa-3* Expression through Intron4

(A) Schematic structures of the deletion constructs of *psa-3::gfp* and their relative level of expression in the T cell granddaughters. ++ indicates that >50% of the animals showed "strong expression" (more than five times higher than background, or "no expression"). + indicates that 10%–50% of the animals showed "strong expression". − indicates no expression or "weak expression" (less than five times higher than "no expression"). Open boxes indicate the coding regions, and the hatched box indicates the i4b region (440 bps). The asterisk indicates the mutation in the NOB-1 binding sequence (TAGT to CGCC).

(B) Summary of the EMSAs and sequences of the probes that were used in them. + or − represent the presence or absence, respectively, of NOB-1 binding. The i4c-S1 or i4c-S2 probes covered site1 or site2 of the I4c region, respectively. Underlined bases indicate the putative binding sequences for CEH-20 (TGA[T or A]). i4c-S2 mut I–V were derived from i4c-S2; mutated residues are shown by bold lower-case letters. The H/P probe contains a canonical Pbx/Hox sequence including TGAT, to which CEH-20 binds, and the H/P Pbx mut probe has mutations in the TGAT sequence.

(C and D) EMSA results. The horizontal arrows indicate shifted bands corresponding to complexes of the NOB-1 proteins and probes. The amounts of the indicated proteins (shown in micrograms), cold oligonucleotides, or antibodies (N, NOB-1 antibody; G, GST antibody) were co-incubated with the indicated probes. WT indicates wild-type i4c-S2 oligonucleotide.

(E) Relative amount of the protein-DNA complex estimated by photo-stimulated luminescence (PSL) by using the BAS2500 system (FUJIFILM). The PSL values were normalized to the control (coincubation of the probe and NOB-1 alone). The means and standard deviations of the relative PSL values obtained in at least three independent experiments were shown. Coincubation with CEH-20 significantly increased the intensities of the shifted bands (*p = 0.01, **p < 0.01, ***p = 0.03 in paired Student's t tests).

sequence is essential for *psa-3* expression in vivo. Taking these data together, we concluded that NOB-1 and CEH-20 directly regulate *psa-3* transcription though intron4.

psa-3/Meis Is Required for the Nuclear Localization of CEH-20/Pbx

We examined *ceh-20* expression by using a *gfp* fusion construct containing the *ceh-20* promoter and the entire coding region. This construct rescued Psa, Unc, and the larval lethal phenotype of *ceh-20* mutants (Table 1). At the L1 stage, *ceh-20* was expressed in nearly all of the cells, including the T cell (Figure 5A; data not shown). During T cell mitosis, CEH-20 was distributed uniformly (data not shown). Soon after T cell division (before V6 division), the nuclear level of CEH-20 was equal in the daughter cells (Figure 5E; early stage in wild-type), while in the late stage, after V6 division, the nuclear level in T.a was slightly greater and that in T.p was slightly less (Figure 5E; late stage in wild-type), resulting in the differential subcellular localization of CEH-20 between the daughter cells (8/33 animals showed the asymmetric
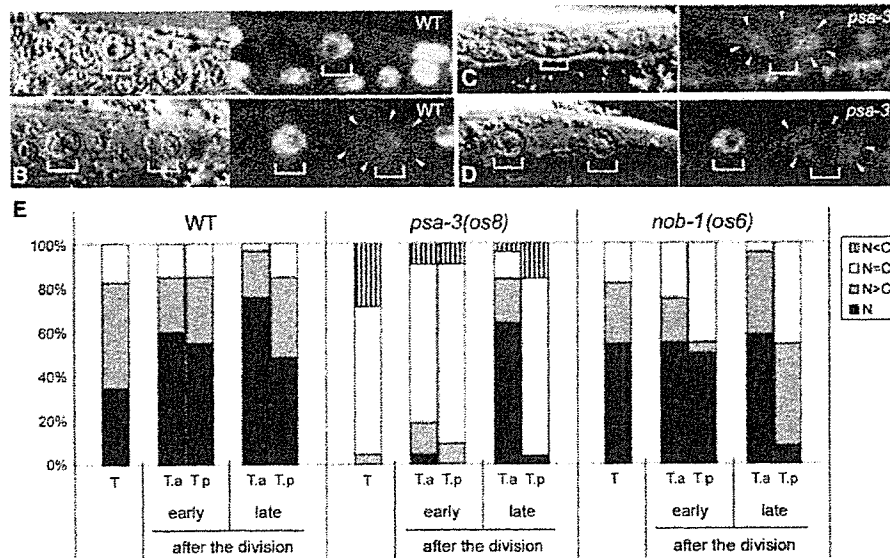
Figure 5. Nuclear Localization of CEH-20 Is Regulated by *psa-3*

(A–D) Expression of *ceh-20::gfp* in the (A) T cell and (B) its daughter cells in wild-type, or in the (C) T cell and (D) its daughter cells in *psa-3(os8)* mutants. White brackets indicate the nucleus of the T cell and its daughters. Arrowheads indicate cell boundaries visualized by the cytoplasmic CEH-20 signal. Anterior is to the left, and ventral is to the bottom.

(E) The subcellular localization of CEH-20 was examined in wild-type, *psa-3(os8)*, or *nob-1(os6)* and was classified into four types: "N" (black bars), "N > C" (gray bars), "N = C" (open bars), and "N < C" (vertical, hatched bars). "N" indicates that CEH-20 exclusively localized to the nucleus. "N > C", "N < C", and "N = C" indicate a difference between the nuclear (N) and cytoplasmic (C) signals. "Early" and "late" indicate before and after the V6 cell division, respectively. In each experiment, more than 20 samples were scored.

localization as shown in Figure 5B; i.e., strong nuclear localization in T.a and weak nuclear and cytoplasmic localization in T.p). These results suggest that the subcellular localization of CEH-20 protein is differentially regulated between the T cell daughters. To investigate the mechanism for the asymmetric nuclear localization, we examined the localization of CEH-20 protein in *psa-3* and *nob-1* mutants. In *psa-3* mutants, the nuclear localization of CEH-20 in the T cell was disrupted (Figures 5C and 5E in *psa-3(os8)* mutants). Soon after the division, the nuclear localization in both daughters was disrupted; however, at the late stage, the nuclear localization of CEH-20 in T.a was normal, but that in T.p was still disrupted (Figure 5E). At this stage, 3/25 animals showed nuclear localization in T.a and preferential cytoplasmic localization in T.p (Figure 5D). This phenotype was not observed in wild-type. Taken together, these data indicate that in both daughters soon after T cell division as well as in the T cell, CEH-20 nuclear localization is regulated by *psa-3*, while at the late stage, CEH-20 nuclear localization in T.p, but not T.a, depends on *psa-3* function. The nuclear localization of CEH-20 in T.a might be regulated by other genes, for example, by another Meis protein, UNC-62 (see Discussion). In *nob-1* mutants, as seen in *psa-3* mutants, the nuclear localization of CEH-20 in T.p was disrupted, albeit partially, in the late stage after division (Figure 5E). This result is consistent with a decreased expression of *psa-3* in the *nob-1* mutants (Figures 3F and 3I).

PSA-3/Meis Functions as a Cell Fate Determinant

The asymmetric expression of *psa-3* between T cell daughters seemed to indicate that PSA-3 functions as a cell fate determinant in T.p (Figures 3B, 3C, and 3H). To test this possibility, we expressed *psa-3* during or just after the T cell division by using a heat shock promoter, and we found that the Psa phenotype of *psa-3* mutants was rescued, albeit partially (Figure 6A). The partial rescue might be because of the lag time between the start of the heat shock treatment and the expression of the PSA-3 protein or because PSA-3 has functions before as well as after the division. In any case, the results suggest that *psa-3* functions in T.p as a cell fate determinant.

In other organisms, Meis family proteins function as cofactors of Pbx and Hox family proteins (Mann and Affolter, 1998). We tested whether PSA-3 can interact physically with CEH-20/Pbx or NOB-1/Hox, as is observed for the Meis proteins in other organisms. We found that GST fusion PSA-3 bound specifically to in vitro-translated CEH-20 (Figure 6B). GST fusion NOB-1 also bound specifically to CEH-20 (Figure 6C). We did not detect significant direct binding between PSA-3 and NOB-1 (Figures 6B and 6C). These results are consistent with the notion that PSA-3 functions as a cofactor for the CEH-20-NOB-1 complex through its binding to CEH-20. Therefore, NOB-1 and CEH-20 not only activate *psa-3* transcription, but may also function with PSA-3 in the cell fate decision. To test this model further, we expressed *psa-3* by using a heat shock promoter in *nob-1* mutants. If *nob-1* was required only for the *psa-3* expression, the expression of *psa-3* should rescue the Psa phenotype of *nob-1* mutants. However, the ectopic expression of *psa-3* rescued the Psa phenotype of *psa-3* mutants, but not that of *nob-1* mutants (Table 1). These results suggested that, even in the presence of PSA-3,
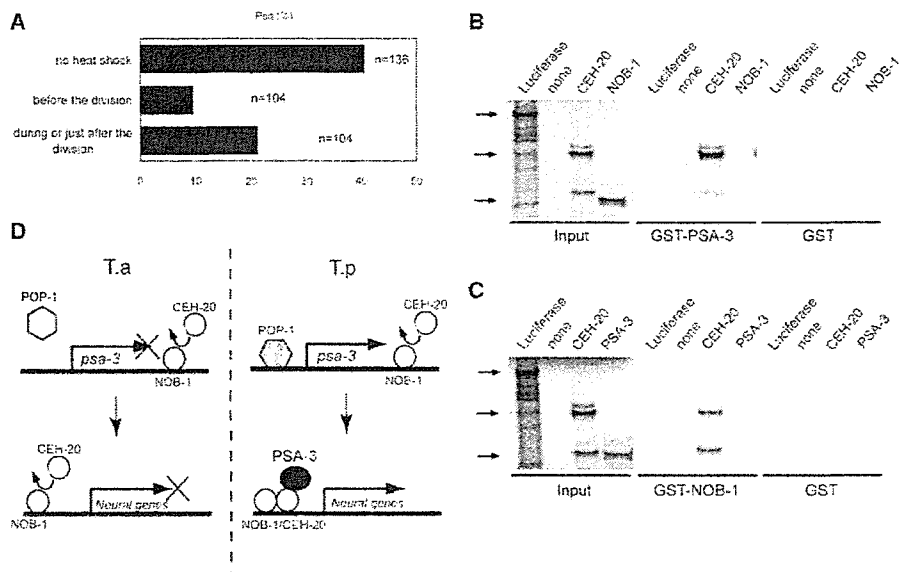
Figure 6. PSA-3 Functions as a Cell Fate Determinant, Probably with CEH-20 and NOB-1

(A) psa-3 can function after the T cell division. Animals containing hsp::PSA-3, whose T cells both on the left and right sides were in mitosis or had just undergone division (as judged by morphology of the nucleus under Nomarski optics), were collected and treated with 1 hr of heat shock at 33°C (during or just after division) or further incubated at 22.5°C as a control (no heat shock). For the "before the division" experiments, the heat shock treatment was started 1 hr after hatching. The heat shock treatment "before the division" and "during or just after the division" significantly rescued the Psa phenotype (p < 0.0001 and p = 0.002 versus "no heat shock", respectively, by Fisher's exact test).

(B and C) In vitro binding assays were performed by using in vitro-translated proteins labeled with [35S]methionine. The arrows indicate in vitro-translated proteins. In the "Input" lanes, we loaded 1/10 of the in vitro-translated protein that we used in the binding assays. The binding assays were performed with (A) GST fusion PSA-3 protein or (B) GST fusion NOB-1 protein. Luciferase or GST proteins were used as negative controls.

(D) A model for the asymmetric T cell division. Asymmetric T cell division results in the activation of POP-1 (hatched hexagon) in T.p; activated POP-1 binds to the psa-3 promoter. psa-3 is selectively induced in T.p by POP-1, and this induction requires the binding of NOB-1 to the psa-3 intronic region, which is promoted by CEH-20. After its induction, PSA-3 forms a complex with NOB-1 and CEH-20, and this complex functions as a cell fate determinant in T.p to induce genes required for the neural fates of its progeny in the tail region. In T.a, PSA-3 is not induced because POP-1 is not active.

NOB-1 function is required for cell fate determination. Taken together, these results support a model in which the PSA-3 protein functions as a cofactor of NOB-1 and CEH-20 to regulate the cell fate of T.p after the asymmetric T cell division (Figure 6D).

Discussion

In this study, we showed that psa-3/Meis expression is regulated by POP-1/TCF, as well as by NOB-1/Hox and CEH-20/Pbx. We also showed that psa-3 can function after the T cell division as a cell fate determinant. POP-1 is a universal factor that determines asymmetry between daughter cells (Herman, 2001; Lin et al., 1998), while NOB-1 regulates the positional identity of cells (Van Auken et al., 2000). Therefore, we conclude that the specific fate of T.p is determined by the cooperation of genes that regulate asymmetric cell division and positional identity, through the induction of psa-3/Meis.

Mechanisms for psa-3/Meis Expression and CEH-20/Pbx Nuclear Localization

In wild-type animals, PSA-3 is expressed before the T cell division, and PSA-3 proteins are inherited equally by the T cell daughters. At the early stage after T cell division, when it is expressed equally in both daughters, PSA-3 is likely to function in the nuclear localization of CEH-20 in both daughter cells. In T.p, nuclear CEH-20 promotes the DNA binding ability of NOB-1, which activates psa-3 transcription in cooperation with POP-1 (Figure 6D). In the late stage after T cell division, when psa-3 expression is induced in T.p, PSA-3 functions to maintain CEH-20's nuclear localization in T.p, while in T.a, CEH-20's nuclear localization does not appear to depend on psa-3 function, because in psa-3 mutants, CEH-20 protein was accumulated normally in the T.a nucleus at the late stage of T cell division (Figures 5D and 5E). In other organisms, the subcellular localization of Pbx family proteins is regulated by their binding with Meis family proteins as well as by phosphorylation by PKC or by direct binding with nonmuscle Myosin (Affolter et al., 1999; Huang et al., 2003; Kilstrup-Nielsen et al., 2003). Similar mechanisms may be used for the nuclear localization of CEH-20 in T.a in C. elegans. Because the CEH-20 nuclear localization is disrupted in T.p, but not in T.a in psa-3 mutants, such psa-3-independent mechanisms are likely to operate only in T.a and hence may be under the control of the Wnt-MAPK pathway.

PSA-3/Meis May Function as a Non-DNA Binding Activator of the CEH-20-Pbx-NOB-1-Hox Complex

Among the Meis family proteins, PSA-3 is unique because it lacks a homeobox. In other organisms, the

requirement of a homeobox for Meis protein function remains controversial. Mutant Meis proteins (Meis1.1 in zebrafish or Homothorax in *Drosophila*) that lack the homeobox act as dominant-negative forms (Ryoo et al., 1999; Waskiewicz et al., 2001). In contrast, mutant Meis3 proteins lacking a homeobox in zebrafish and *Xenopus* do not show dominant-negative effects and can even activate Pbx-Hox-dependent transcription in vivo (Choe et al., 2002; Salzberg et al., 1999). In addition, mutant Meis proteins (Meis1A or Prep1) that do not bind DNA can enhance the DNA binding activity of the Hox-Pbx complex in vitro (Berthelsen et al., 1998; Shanmugam et al., 1999). In *Drosophila*, deletion of the homeobox in the *homothorax* gene causes only partial and weak defects in the peripheral nervous system, whereas mutations affecting the Meis domain cause much more severe phenotypes. Given these observations, it was proposed that the homeobox-less Homothorax retains some of its transcription-regulating function via its interaction with Extradenticle/Pbx (Kurant et al., 2001). In our study, loss-of-function mutants of *psa-3*, *ceh-20*, or *nob-1* had the same defect in the asymmetric T cell division. Therefore, although PSA-3 lacks a homeobox, it is likely that it positively regulates CEH-20 and NOB-1 rather than inhibiting them by acting as a dominant-negative form. For example, although CEH-20 did not stably bind to DNA with NOB-1, at least in our EMSA experiments, PSA-3 may stabilize their interaction. In this model, PSA-3 induced in a T.p cell stabilizes the CEH-20-NOB-1 complex on DNA, while in a T.a cell, CEH-20 cannot stably interact with DNA (Figure 6D). Further analyses are necessary to clarify the roles of PSA-3 in cell fate determination.

Do *Hox* Genes Regulate Asymmetric Cell Division in Vertebrates?

In this study, we showed that cooperation between the mechanisms for asymmetric cell division and positional identity determines the specific cell fate in asymmetric T cell division in *C. elegans*. Such cooperation may explain how the general mechanism for asymmetric division specifies individual cell fates in other organisms. In vertebrates, *Hox* genes play essential roles in the development of the segmental pattern of the central nervous system. They also regulate the segmental identities of specific neurons. In the hindbrain, *Hox* genes are involved in the fate determination of specific motor neurons, such as branchial and somatic motoneurons and sensory interneurons, like the visceral and somatic sensory interneurons (Gaufo et al., 2003, 2004; Samad et al., 2004). In the spinal cord, the identities of the unique motor neurons in individual segmental domains are determined by *Hox* genes (Dasen et al., 2003). During neurogenesis, neurons are generated through the asymmetric divisions of neuroepithelial cells or neuronal progenitor cells (Chenn and McConnell, 1995; Kosodo et al., 2004). Therefore, it is possible that *Hox* genes regulate the segmental specificities of neurons when they are generated by asymmetric cell divisions in vertebrate neurogenesis.

Similarly, some Hox, Pbx, and Meis proteins are expressed and function in hematopoietic stem cells (HSCs) and in specific hematopoietic cell lineages (Di-Martino et al., 2001; Hisa et al., 2004; Pineault et al.,

2002). Although it remains to be proved, some studies have suggested that HSCs undergo asymmetric cell division (Denkers et al., 1993; Ema et al., 2000; Ho, 2005; Takano et al., 2004). Thus, Hox proteins and their cofactors may specify hematopoietic lineages upon asymmetric cell division in a manner that is similar to the one we have described here for the T cell in *C. elegans*.

Experimental Procedures

Genetic Experiments
Methods for the culture and genetic manipulation of *C. elegans* were as described (Brenner, 1974; Sawa et al., 2000). The Psa phenotype was determined as described (Sawa et al., 2000). Fluorescence from GFP fusion proteins was observed with a confocal microscope (LSM510 system by Carl Zeiss), and the intensity of the GFP fluorescence was measured by the system's software. RNAi assays for *psa-3* were carried out by microinjecting double-stranded RNAs synthesized by using part of exon4 (~200 bp fragment of yk375g3) (Fire et al., 1998). To map *psa-3*, we isolated recombinants from *unc-7 lin-15/psa-3(os8)*. Five of 14 Unc non-Lin recombinants segregated with *psa-3*. Seven of ten Lin non-Unc recombinants segregated with *psa-3*. The deletion in *psa-3(os8)* was located between −514 and −256 bps, and the point mutation was at −185 bp upstream of the initiation codon in exon1α. The deletions in *tm656* and *tm657* are described in the National BioResource Project (http://www.nbrp.jp/report/reportProject.jsp?project=celegans).

Plasmid Construction
A 14 kb Bst1107I fragment of F39D8 was subcloned into pBSK to produce pPS3.11. A 5 kb BsmI fragment containing the *pqn-36* gene was removed from pPS3.11 to generate pPS3.16. To generate *psa-3::gfp*, the entire *psa-3* coding region within pPS3.16 was subcloned into a GFP vector, pPD95.77 (a gift from Dr. A. Fire, Stanford University, Stanford, CA), after removal of the 3' UTR region containing the stop codon. *mut-psa-3::gfp*, shown in Figure 3D, and Δ4 to TAGT*mut*, shown in Figure 4A, were made by a PCR-based method, and their sequences were confirmed by direct sequencing. *hsp::PSA-3* and *hsp::PSA-3::gfp* were constructed by subcloning the *psa-3* cDNA or the *gfp* fusion *psa-3* cDNA, respectively, whose product was GFP joined to the C terminus of PSA-3, into pPD49.78 (a gift from Dr. A. Fire). For the heat shock experiments, animals were incubated at 33°C for 1 hr and overnight at 22.5°C. *ceh-20::gfp* was constructed by inserting a *gfp* fragment from pPD118.90 (a gift from Dr. A. Fire) into a PstI site in exon4 of the *ceh-20* gene (the rescuing plasmid was a gift from Dr. M. Stern, Yale University, New Haven, CT).

In Vitro Binding Assay and EMSA
For the GST fusion proteins or hexahistidine-tagged proteins, the cDNAs of *psa-3*, *ceh-20*, and *nob-1* in yk375g3, yk219d9, and yk467d4, respectively, were subcloned into pGex6P or pQE-82L (Amersham and QIAGEN). yk219d9 was used after removal of the 5' region, as described (Liu and Fire, 2000). Purification of proteins expressed in *E. coli* (BL-21) and in vitro binding assays was performed as described (Tomoda et al., 1999). ^{35}S-labeled proteins were synthesized by the TNT T7/T3-coupled Reticulocyte Lysate System (Promega). EMSAs were performed by using probes labeled with α-^{32}P-dCTP by the Klenow fragment (Asubel et al., 1996). Rabbit antibody against NOB-1 was produced by using GST fusion NOB-1 protein.

Supplemental Data
Supplemental Data include one table and are available at http://www.developmentalcell.com/cgi/content/full/11/1/105/DC1/.

and L. Tuda, T. Yamamoto, I. Matsuo, S. Kuraku, and members of the Sawa laboratory for helpful discussions and comments. This work was supported by the Special Postdoctoral Researchers Program, Riken (Y.A.); by a grant from the Japanese Ministry of Education, Culture, Sports, Science and Technology; and by National Institutes of Health grant GM56339 (M.A.H).

References

Affolter, M., Marty, T., and Vigano, M.A. (1999). Balancing import and export in development. Genes Dev. *13*, 913–915.

Asubel, F.M., Brent, R., Kingston, R.E., Moore, D.D., Seidman, J.G., Smith, J.A., and Struhl, K. (1996). Current Protocols in Molecular Biology, Volume 2 (New York: John Wiley and Sons, Inc.).

Berger, C., Pallavi, S.K., Prasad, M., Shashidhara, L.S., and Technau, G.M. (2005). A critical role for *cyclin E* in cell fate determination in the central nervous system of *Drosophila melanogaster*. Nat. Cell Biol. *7*, 56–62.

Berthelsen, J., Zappavigna, V., Ferretti, E., Mavilio, F., and Blasi, F. (1998). The novel homeoprotein Prep1 modulates Pbx-Hox protein cooperativity. EMBO J. *17*, 1434–1445.

Bhat, K.M. (1999). Segment polarity genes in neuroblast formation and identity specification during *Drosophila* neurogenesis. Bioessays *21*, 472–485.

Brenner, S. (1974). The genetics of *Caenorhabditis elegans*. Genetics *77*, 71–94.

Burglin, T.R. (1997). Analysis of TALE superclass homeobox genes (MEIS, PBC, KNOX, Iroquois, TGIF) reveals a novel domain conserved between plants and animals. Nucleic Acids Res. *25*, 4173–4180.

Chenn, A., and McConnell, S.K. (1995). Cleavage orientation and the asymmetric inheritance of Notch1 immunoreactivity in mammalian neurogenesis. Cell *82*, 631–641.

Choe, S.K., Vlachakis, N., and Sagerstrom, C.G. (2002). Meis family proteins are required for hindbrain development in the zebrafish. Development *129*, 585–595.

Dasen, J.S., Liu, J.P., and Jessell, T.M. (2003). Motor neuron columnar fate imposed by sequential phases of Hox-c activity. Nature *425*, 926–933.

Denkers, I.A., Dragowska, W., Jaggi, B., Palcic, B., and Lansdorp, P.M. (1993). Time lapse video recordings of highly purified human hematopoietic progenitor cells in culture. Stem Cells *11*, 243–248.

DiMartino, J.F., Selleri, L., Traver, D., Firpo, M.T., Rhee, J., Warnke, R., O'Gorman, S., Weissman, I.L., and Cleary, M.L. (2001). The Hox cofactor and proto-oncogene Pbx1 is required for maintenance of definitive hematopoiesis in the fetal liver. Blood *98*, 618–626.

Ema, H., Takano, H., Sudo, K., and Nakauchi, H. (2000). *In vitro* self-renewal division of hematopoietic stem cells. J. Exp. Med. *192*, 1281–1288.

Fire, A., Xu, S., Montgomery, M.K., Kostas, S.A., Driver, S.E., and Mello, C.C. (1998). Potent and specific genetic interference by double-stranded RNA in *Caenorhabditis elegans*. Nature *391*, 806–811.

Gaufo, G.O., Thomas, K.R., and Capecchi, M.R. (2003). *Hox3* genes coordinate mechanisms of genetic suppression and activation in the generation of branchial and somatic motoneurons. Development *130*, 5191–5201.

Gaufo, G.O., Wu, S., and Capecchi, M.R. (2004). Contribution of *Hox* genes to the diversity of the hindbrain sensory system. Development *131*, 1259–1266.

Herman, M. (2001). *C. elegans* POP-1/TCF functions in a canonical Wnt pathway that controls cell migration and in a noncanonical Wnt pathway that controls cell polarity. Development *128*, 581–590.

Herman, M.A. (2002). Control of cell polarity by noncanonical Wnt signaling in *C. elegans*. Semin. Cell Dev. Biol. *13*, 233–241.

Hisa, T., Spence, S.E., Rachel, R.A., Fujita, M., Nakamura, T., Ward, J.M., Devor-Henneman, D.E., Saiki, Y., Kutsuna, H., Tessarollo, L., et al. (2004). Hematopoietic, angiogenic and eye defects in Meis1 mutant animals. EMBO J. *23*, 450–459.

Ho, A.D. (2005). Kinetics and symmetry of divisions of hematopoietic stem cells. Exp. Hematol. *33*, 1–8.

Huang, H., Paliouras, M., Rambaldi, I., Lasko, P., and Featherstone, M. (2003). Nonmuscle myosin promotes cytoplasmic localization of PBX. Mol. Cell. Biol. *23*, 3636–3645.

Jan, Y.N., and Jan, L.Y. (2001). Asymmetric cell division in the *Drosophila* nervous system. Nat. Rev. Neurosci. *2*, 772–779.

Kaletta, T., Schnabel, H., and Schnabel, R. (1997). Binary specification of the embryonic lineage in *Caenorhabditis elegans*. Nature *390*, 294–298.

Kenyon, C.J., Austin, J., Costa, M., Cowing, D.W., Harris, J.M., Honigberg, L., Hunter, C.P., Maloof, J.N., Muller-Immergluck, M.M., Salser, S.J., et al. (1997). The dance of the *Hox* genes: patterning the anteroposterior body axis of *Caenorhabditis elegans*. Cold Spring Harb. Symp. Quant. Biol. *62*, 293–305.

Kidd, A.R., 3rd, Miskowski, J.A., Siegfried, K.R., Sawa, H., and Kimble, J. (2005). A beta-catenin identified by functional rather than sequence criteria and its role in Wnt/MAPK signaling. Cell *121*, 761–772.

Kilstrup-Nielsen, C., Alessio, M., and Zappavigna, V. (2003). PBX1 nuclear export is regulated independently of PBX-MEINOX interaction by PKA phosphorylation of the PBC-B domain. EMBO J. *22*, 89–99.

Koh, K., Peyrot, S.M., Wood, C.G., Wagmaister, J.A., Maduro, M.F., Eisenmann, D.M., and Rothman, J.H. (2002). Cell fates and fusion in the *C. elegans* vulval primordium are regulated by the EGL-18 and ELT-6 GATA factors–apparent direct targets of the LIN-39 Hox protein. Development *129*, 5171–5180.

Kosodo, Y., Roper, K., Haubensak, W., Marzesco, A.M., Corbeil, D., and Huttner, W.B. (2004). Asymmetric distribution of the apical plasma membrane during neurogenic divisions of mammalian neuroepithelial cells. EMBO J. *23*, 2314–2324.

Kurant, E., Eytan, D., and Salzberg, A. (2001). Mutational analysis of the *Drosophila* homothorax gene. Genetics *157*, 689–698.

Lin, R., Hill, R.J., and Priess, J.R. (1998). POP-1 and anterior-posterior fate decisions in *C. elegans* embryos. Cell *92*, 229–239.

Liu, J., and Fire, A. (2000). Overlapping roles of two Hox genes and the exd ortholog *ceh-20* in diversification of the *C. elegans* postembryonic mesoderm. Development *127*, 5179–5190.

Mann, R.S., and Affolter, M. (1998). Hox proteins meet more partners. Curr. Opin. Genet. Dev. *8*, 423–429.

Pineault, N., Helgason, C.D., Lawrence, H.J., and Humphries, R.K. (2002). Differential expression of *Hox*, *Meis1*, and *Pbx1* genes in primitive cells throughout murine hematopoietic ontogeny. Exp. Hematol. *30*, 49–57.

Ryoo, H.D., Marty, T., Casares, F., Affolter, M., and Mann, R.S. (1999). Regulation of Hox target genes by a DNA bound Homothorax/Hox/Extradenticle complex. Development *126*, 5137–5148.

Saitou, N., and Nei, M. (1987). The neighbor-joining method: a new method for reconstructing phylogenetic trees. Mol. Biol. Evol. *4*, 406–425.

Salser, S.J., and Kenyon, C. (1996). A *C. elegans* Hox gene switches on, off, on and off again to regulate proliferation, differentiation and morphogenesis. Development *122*, 1651–1661.

Salzberg, A., Elias, S., Nachaliel, N., Bonstein, L., Henig, C., and Frank, D. (1999). A Meis family protein caudalizes neural cell fates in *Xenopus*. Mech. Dev. *80*, 3–13.

Samad, O.A., Geisen, M.J., Caronia, G., Varlet, I., Zappavigna, V., Ericson, J., Goridis, C., and Rijli, F.M. (2004). Integration of anteroposterior and dorsoventral regulation of Phox2b transcription in cranial motoneuron progenitors by homeodomain proteins. Development *131*, 4071–4083.

Sawa, H., Kouike, H., and Okano, H. (2000). Components of the SWI/SNF complex are required for asymmetric cell division in *C. elegans*. Mol. Cell *6*, 617–624.

Shanmugam, K., Green, N.C., Rambaldi, I., Saragovi, H.U., and Featherstone, M.S. (1999). PBX and MEIS as non-DNA-binding partners in trimeric complexes with HOX proteins. Mol. Cell. Biol. 19, 7577–7588.

Shen, W.F., Rozenfeld, S., Lawrence, H.J., and Largman, C. (1997). The Abd-B-like Hox homeodomain proteins can be subdivided by the ability to form complexes with Pbx1a on a novel DNA target. J. Biol. Chem. 272, 8198–8206.

Shetty, P., Lo, M.C., Robertson, S.M., and Lin, R. (2005). C. elegans TCF protein, POP-1, converts from repressor to activator as a result of Wnt-induced lowering of nuclear levels. Dev. Biol. 285, 584–592.

Streit, A., Kohler, R., Marty, T., Belfiore, M., Takacs-Vellai, K., Vigano, M.A., Schnabel, R., Affolter, M., and Muller, F. (2002). Conserved regulation of the Caenorhabditis elegans labial/Hox1 gene ceh-13. Dev. Biol. 242, 96–108.

Takano, H., Ema, H., Sudo, K., and Nakauchi, H. (2004). Asymmetric division and lineage commitment at the level of hematopoietic stem cells: inference from differentiation in daughter cell and granddaughter cell pairs. J. Exp. Med. 199, 295–302.

Takeshita, H., and Sawa, H. (2005). Asymmetric cortical and nuclear localizations of WRM-1/beta-catenin during asymmetric cell division in C. elegans. Genes Dev. 19, 1743–1748.

Thorpe, C.J., Schlesinger, A., and Bowerman, B. (2000). Wnt signalling in Caenorhabditis elegans: regulating repressors and polarizing the cytoskeleton. Trends Cell Biol. 10, 10–17.

Tomoda, K., Kubota, Y., and Kato, J. (1999). Degradation of the cyclin-dependent-kinase inhibitor p27Kip1 is instigated by Jab1. Nature 398, 160–165.

Van Auken, K., Weaver, D.C., Edgar, L.G., and Wood, W.B. (2000). Caenorhabditis elegans embryonic axial patterning requires two recently discovered posterior-group Hox genes. Proc. Natl. Acad. Sci. USA 97, 4499–4503.

Van Auken, K., Weaver, D., Robertson, B., Sundaram, M., Saldi, T., Edgar, L., Elling, U., Lee, M., Boese, Q., and Wood, W.B. (2002). Roles of the Homothorax/Meis/Prep homolog UNC-62 and the Exd/Pbx homologs CEH-20 and CEH-40 in C. elegans embryogenesis. Development 129, 5255–5268.

Waskiewicz, A.J., Rikhof, H.A., Hernandez, R.E., and Moens, C.B. (2001). Zebrafish Meis functions to stabilize Pbx proteins and regulate hindbrain patterning. Development 128, 4139–4151.

Zhao, X., Yang, Y., Fitch, D.H., and Herman, M.A. (2002). TLP-1 is an asymmetric cell fate determinant that responds to Wnt signals and controls male tail tip morphogenesis in C. elegans. Development 129, 1497–1508.

Accession Numbers

Enhanced neurogenesis in the ischemic striatum following EGF-induced expansion of transit-amplifying cells in the subventricular zone

Mikiko Ninomiya [a,b,c,e], Toru Yamashita [a,b,d,e], Nobuo Araki [c],
Hideyuki Okano [b,e], Kazunobu Sawamoto [a,b,e,*]

[a] Bridgestone Laboratory of Developmental and Regenerative Neurobiology, Keio University School of Medicine,
35 Shinanomachi, Shinjuku, Tokyo 160-8582, Japan
[b] Department of Physiology, Keio University School of Medicine, Tokyo 160-8582, Japan
[c] Department of Neurology, Saitama Medical School, Saitama 350-0495, Japan
[d] Department of Neurology, Okayama University Graduate School of Medicine, Dentistry and Pharmaceutical Sciences,
Okayama 700-8558, Japan
[e] Core Research for Evolutional Science and Technology (CREST), Japan Science and Technology Agency (JST), Saitama 332-0012, Japan

Abstract

In the subventricular zone (SVZ) of the adult mammalian brain, neural stem cells continually produce transit-amplifying precursors, which generate neuroblasts migrating into the olfactory bulb. Previous studies have suggested that SVZ cells also have the capacity to generate some striatal neurons after cerebral ischemia. The infusion of epidermal growth factor (EGF) has been demonstrated to increase the number of these regenerated neurons. However, which cell types in the SVZ are stimulated to proliferate or differentiate after EGF infusion remains unknown. In this paper, we demonstrated that cerebral ischemia results in an increase in the number of EGF receptor (EGFR)-positive transit-amplifying cells in the SVZ. EGF infusion into the ischemic brain caused the number of transit-amplifying cells to increase and the number of neuroblasts to decrease. On the other hand, after an interval of 6 days after the discontinuation of EGF infusion, a significant increase in the number of neuroblasts was found, both in the striatum and the SVZ. These results suggest that the replacement of neurons in injured striatum can be enhanced by an EGF-induced expansion of transit-amplifying cells in the SVZ.
© 2006 Elsevier Ireland Ltd. All rights reserved.

Keywords: EGF; Cerebral ischemia; Neurogenesis

Neurogenesis continues in two restricted regions of the adult mammalian brain: the subventricular zone (SVZ) of the lateral ventricles [1] and the dentate gyrus of the hippocampus [9]. In the SVZ, astrocytes have been identified as neural stem cells [6]; dividing astrocytes give rise to transit-amplifying cells that differentiate into neuroblasts. In the intact brain, most of these neuroblasts migrate toward the olfactory bulb, where they differentiate into local interneurons [13,14].

Previous studies in animal models of middle cerebral artery occlusion (MCAO) have suggested that cerebral ischemia results in an increase in the number of neuroblasts in the SVZ and in their migration into the injured striatum [2,15]. However, these neuroblasts give rise to only a small number of striatal neurons

that do not support functional recovery [2]. On the other hand, the stimulation of neural progenitors in the SVZ using various growth factors and/or neurotrophic factors has been shown to significantly increase their proliferation and migration into the intact striatum [12]. For example, EGF infusion into intact brain caused cell migration from the SVZ to the striatum. These cells, despite being non-neurogenic, differentiated into glial cells [5,8,11]. In contrast, EGF infusion into ischemic brain increased the number of new neurons in the injured striatum several weeks after the discontinuation of the infusion [20]. However, the early effects of EGF on SVZ cells in ischemic brain have not been demonstrated. In this study, we determined the expression pattern of the EGF receptors (EGFR) in the SVZ after MCAO. We also examined the effects of EGF infusion on the number of transit-amplifying cells and neuroblasts in the ischemic brain. Our results indicated that the effects of EGF on the SVZ of ischemic brains occur in at least two stages: (i) the expansion

* Corresponding author. Tel.: +81 3 5363 3747; fax: +81 3 3357 5445.
E-mail address: sawamoto@sc.itc.keio.ac.jp (K. Sawamoto).

of transit-amplifying cells in the SVZ in the presence of EGF; and (ii) the differentiation of these cells into neuroblasts after the discontinuation of EGF infusion.

Adult ICR mice (25–30 g) were purchased from SLC (Japan). The animals were maintained under a 12-hour light/dark cycle and were allowed unlimited access to food and water.

Before the surgery, the mice were anesthetized with a nitrous oxide/oxygen/isoflurane mixture (69/30/1%) administered through an inhalation mask. The rectal temperature was maintained at 37.0 °C by placing the animals on a heating bed (Model BMT-100; Bio Research Center).

Middle cerebral artery occlusion was accomplished using the previously described intraluminal filament technique [23]. A laser Doppler flowmeter probe (Model ALF21; ADVANCE) was attached to the surface of the ipsilateral cortex to monitor the regional cerebral blood flow. Thirty minutes later, the silicone-coated 8-0 filament was withdrawn, and reperfusion was confirmed by laser-Doppler flowmetry.

Human recombinant EGF (Sigma) (400 ng/day) dissolved in 0.9% saline containing 1 mg/ml of mouse serum albumin (Sigma) or vehicle alone was infused into the brain parenchyma close to the SVZ (2.5 mm lateral to the bregma and at a depth of 3.0 mm from the scalp) using an osmotic pump (Alzet, model 1002; flow rate, 0.25 μl/h) and a brain infusion kit 3 (Alzet). EGF was infused continuously for 7 days starting at 5 days after the induction of ischemia. The mice were sacrificed immediately after the discontinuation of the infusion (12 days after the induction of ischemia) or 6 days after the removal of the infusion pump (18 days after the induction of ischemia) (Fig. 2).

The brains were perfusion-fixed with 4% paraformaldehyde (PFA), post-fixed in the same fixative for two consecutive nights, and cut into 50-μm sections using a vibratome. After being rinsed thrice in PBS, the sections were incubated for 1 h in TNB blocking solution (Vector Laboratories), overnight with the primary antibodies, and for 2 h at room temperature with a biotinylated secondary antibody (1:500) or an Alexa Fluor-conjugated secondary antibody (1:500, Molecular Probes), unless otherwise specified. The biotinylated antibodies were visualized using the Vectastain Elite ABC kit (Vector Laboratories) or the tyramide signal amplification (TSA) kit (PerkinElmer Life Science). The primary antibodies (final dilution and source) used in this study were sheep polyclonal anti-EGFR (1:500, Upstate), mouse monoclonal anti-GFAP (1:100, Sigma), mouse monoclonal anti-Mash1 (1:100, Pharmingen), and goat anti-Doublecortin (DCX) (1:100, Santa Cruz). The nuclei were stained with Hoechst 33258.

Photographs were obtained using a confocal laser microscope (LSM510; Carl Zeiss). The cell numbers on the entire length of the lateral wall of the lateral ventricle were counted using three optical sections of the caudate-putamen (1.0, 0.5, and 0 mm rostral to the bregma) from each animal.

Values were expressed as the mean ± S.E. An ANOVA with the Tukey correction (Fig. 1) or an unpaired t-test (Fig. 2) was used to evaluate the significance of the differences.

In our MCAO model [23], the infarct damage was consistently located on the lateral side of the striatum, including the cortex (Fig. 1 A). We examined the expression pattern of the

EGF receptors (EGFR) in the SVZ at 0, 2, 4, 7, and 14 days after the induction of ischemia. The number of EGFR-positive cells was significantly increased in the SVZ of the ischemic brain on Day 7 (Fig. 1 B) and Day 14 (data not shown), compared with that in the normal brain. A previous study [20] reported a similar but slightly earlier peak of EGFR expression after MCAO; this difference was probably caused by differences in the length of the occlusion periods and the mouse strains that were used. To identify these EGFR-positive cells, we stained the sections of the SVZ obtained on Day 7 with antibodies against Mash1 (for transit-amplifying cells; [17]), GFAP (for astrocytes; [7]), or DCX (for neuroblasts; [3]), in combination with EGFR. Mash1-immunopositive cells are highly mitotic, express Dlx (a marker for transit-amplifying cells and neuroblasts [8]), and do not express markers for neroblasts or astrocytes in the SVZ (Toida et al., personal communication; [17]), indicating that they are transit-amplifying cells. Of the total EGFR-positive cells in the ischemic SVZ ($n = 500$; three mice), 320 cells (64.0%) were Mash1-positive transit-amplifying cells, similar to the previously reported number in intact SVZ [8,10]. EGFR signals were also detected in a small subset of GFAP+ SVZ astrocytes (data not shown), although their distinct subcellular localization prevented quantitative analysis. EGFR was not detected in the DCX+ neuroblasts (Fig. 1 D) or ependymal cells lining the ventricular wall (data not shown). The number of EGFR+/Mash1+ double-positive cells in the SVZ significantly increased on Day 7 and Day 14 after MCAO (Fig. 1 E). Therefore, this expanded population of EGFR-positive transit-amplifying cells likely responded to the EGF infusion.

Based on this timing of the increase in the number of EGFR+/Mash1+ cells (Fig. 1), we administered EGF into the brain parenchyma close to the SVZ between Day 5 and Day 12 after the induction of ischemia. We did not observe any difference in the number of DCX-positive cells between saline-infused brain and control (data not shown), indicating that neurogenesis was not affected by any physical damage caused by the insertion of the osmotic pump. To study the early and late effects of EGF infusion separately, the mice were sacrificed for analyses on Day 12 or Day 18 (Fig. 2). On Day 12, hypercellular polyps were observed (data not shown) on the lateral ventricular wall, as reported previously [4,11], indicating that the EGF infusion induced the cells in the SVZ to proliferate. In the animals that received EGF, the number of Mash1+ cells in the SVZ increased on Day 12 after the induction of ischemia (2.26-fold increase; 262 ± 8 versus 116 ± 12; $p < 0.01$) (Fig. 2 A and C). We also noted that EGF-infusion caused an increase of GFAP+ astrocytes, although the subcellular localization of GFAP and the complex morphology of the astrocytes prevented quantitative analyses. In contrast, the number of DCX+ cells (neuroblasts) in the SVZ significantly decreased (87% decrease; 27 ± 5 versus 210 ± 13; $p < 0.05$) on Day 12 after MCAO in these animals (Fig. 2 D and F). The contralateral SVZ was not affected by EGF infusion (data not shown). These results suggest that while EGF infusion stimulated the proliferation of the transit-amplifying cells, it inhibited their differentiation into neuroblasts. It is also possible that the EGF-induced decrease in the number of DCX+